Supporting Information

Comparing Alkene-mediated and Formaldehyde-mediated Diene Formation Routes in Methanol-to-Olefins Catalysis in MFI and CHA

Lauren Kilburn, Mykela DeLuca, Alexander Hoffman, Shivang Patel, David Hibbitts*

Department of Chemical Engineering, University of Florida, Gainesville, 32611

*Corresponding author: hibbitts@che.ufl.edu

Table of Contents
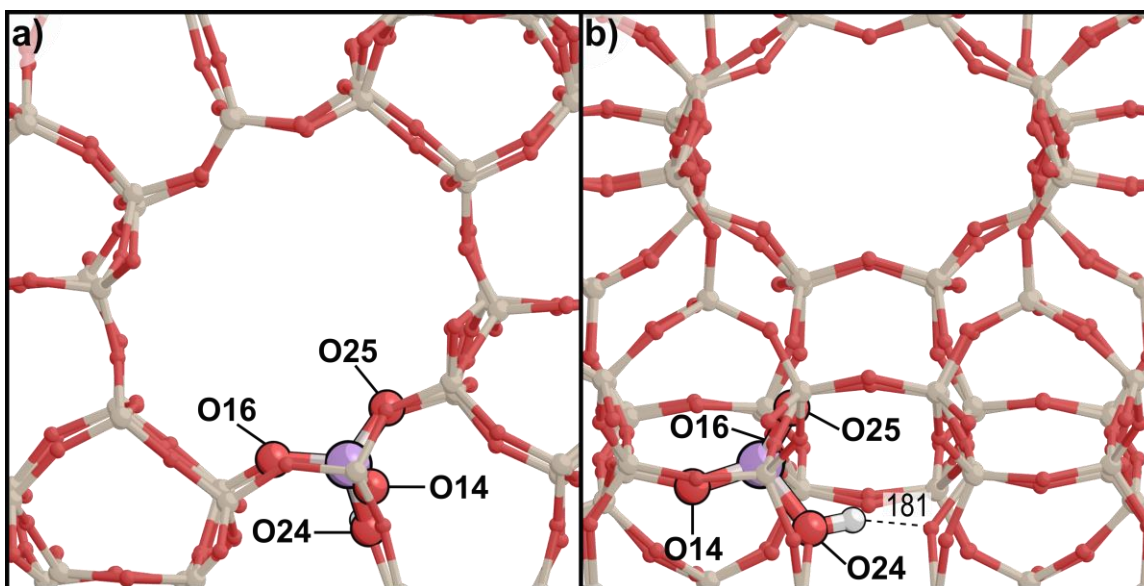
S1. Details of Framework Structures

Figure S1. a) Straight and b) sinusoidal view of HZSM-5 (MFI) structure.
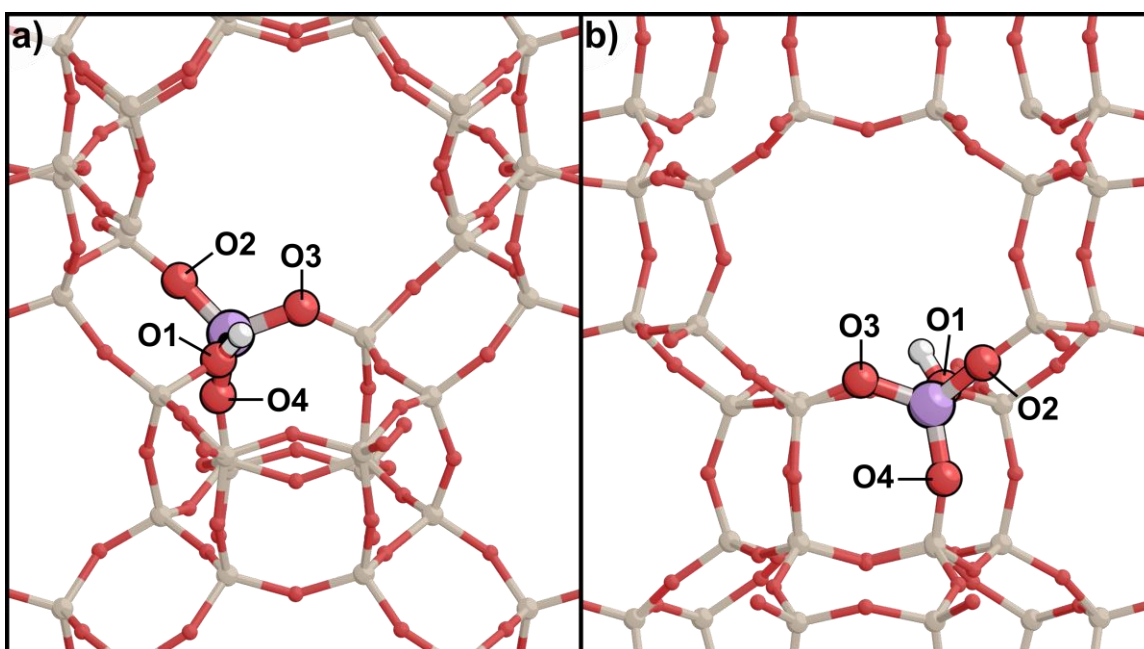

Figure S2. a) Front and b) back view of H-SSZ-13 (CHA) structure.

S2. Frequency Calculations for Temperature-Corrected Enthalpies and Entropies

Frequency calculations are normal mode analyses and were performed on all optimization and Dimer calculations. Frequency calculations were used to determine zero-point vibrational energy (ZPVE), vibrational enthalpy (H_{vib}), and vibrational free energy (G_{vib}) for adsorbed species to calculate enthalpy (H):

$$H = E_0 + ZPVE + H_{vib} \tag{S1}$$

and free energy (G):

$$G = E_0 + ZPVE + G_{vib} \tag{S2}$$

Translational and rotational enthalpies and free energies are also calculated for gas phase species to compute gas phase enthalpy:

$$H = E_0 + ZPVE + H_{vib} + H_{rot} + H_{trans} \tag{S3}$$

and gas phase free energy:

$$G = E_0 + ZPVE + H_{vib} + H_{rot} + H_{trans} \tag{S4}$$

S3. Derivation of Maximum Rates of Diene Formation Reactions

Maximum rate analysis is employed to compare the rate of reactions with different pressure dependencies and to determine the overall rate of the alkene-mediated and CH_2O-mediated pathways. Rates are calculated for each step of the pathway using transition state theory by asserting that step as rate determining and assuming all prior reactions are quasi-equilibrated. All adsorptions are assumed to be quasi-equilibrated, and all subsequent steps are considered kinetically irrelevant.

Potential most abundant surface intermediates (MASI) considered for alkene-mediated rates are [*], C_2H_4*, C_4H_8*, C_4H_8*--C_2H_4*, C_2H_5–Z, and C_4H_8--C_2H_5–Z. The site balance is given as:

$$\frac{[*]}{[L]} = (1 + K_{C_2H_4}(C_2H_4) + K_{C_4H_8}(C_4H_8) + K_{C_2H_4}K_{C_4H_8-C_2H_4}(C_4H_8)(C_2H_4) + K_{S1}(C_2H_4)$$
$$+ K_{C_4H_8-C_2H_5-Z}K_{S1}(C_4H_8)(C_2H_4) \tag{S5}$$

where $K_{C_xH_y}$ represents the rate constant of equilibrated adsorption, and K_{S1} represents the rate constant of equilibrated C_2H_5–Z formation, and species in parentheses represent partial pressures. The term [*] represents all empty sites and the term [L] represents all possible sites.

The first step of the sequential mechanism for the alkene-mediated route, C_2H_5–Z formation, consists of two steps:

$$C_2H_4(g) + * \rightleftharpoons C_2H_4{}^* \qquad\qquad K_{C_2H_4} \tag{S6}$$

$$C_2H_4{}^* \rightarrow C_2H_5-Z \qquad\qquad k_{S1} \qquad\qquad \text{(S7)}$$

The rate of C_2H_5–Z formation is given by:

$$r = k_{S1}[C_2H_4{}^*] \qquad\qquad \text{(S8)}$$

The rate described in Eq. 8 can be written using partial pressures by combining Eqs. S5 and S6.

$$r = K_{C_2H_4}k_{S1}(C_2H_4)[*] \qquad\qquad \text{(S9)}$$

Normalizing the rate by the number of sites [L], yields this generalized form of the rate equation:

$$\frac{r}{L} = K_{C_2H_4}k_{S1}(C_2H_4)\left(\frac{[*]}{L}\right) \qquad\qquad \text{(S10)}$$

The first step can also occur with spectating C_4H_8 and consists of three steps:

$$C_2H_4(g) + * \rightleftharpoons C_2H_4{}^* \qquad\qquad K_{C_2H_4} \qquad\qquad \text{(S11)}$$

$$C_4H_8(g) + C_2H_4{}^* \rightleftharpoons C_4H_8-C_2H_4{}^* \qquad\qquad K_{C_4H_8-C_2H_4} \qquad\qquad \text{(S12)}$$

$$C_4H_8-C_2H_4{}^* \rightarrow C_4H_8-C_2H_5-Z \qquad\qquad k_{S1\,S} \qquad\qquad \text{(S13)}$$
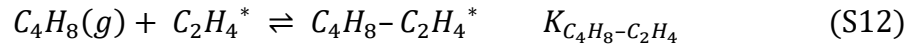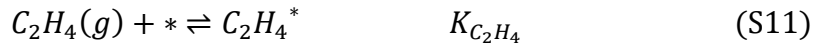
The rate of C_2H_5–Z formation with spectating C_4H_8 is given by:

$$r = k_{S1\,S}[C_4H_8-C_2H_4{}^*] \qquad\qquad \text{(S14)}$$

The rate equation (Eq. S14) can be combined with Eqs. S5, S11, and S12 to yield:

$$r = K_{C_2H_4}K_{C_4H_8-C_2H_4}k_{S1\,S}(C_2H_4)(C_4H_8)[*] \qquad\qquad \text{(S15)}$$

And normalized by the number of sites [L]:

$$\frac{r}{L} = K_{C_2H_4}K_{C_4H_8-C_2H_4}k_{S1\,S}(C_2H_4)(C_4H_8)\left(\frac{[*]}{[L]}\right) \qquad\qquad \text{(S16)}$$

The second step of the sequential alkene-mediated route, the C_2H_5–Z hydride transfer, requires four steps. Assuming that C_4H_8 adsorption occurs after C_2H_5–Z formation:

$$C_2H_4(g) + * \rightleftharpoons C_2H_4{}^* \qquad\qquad K_{C_2H_4} \qquad\qquad \text{(S17)}$$

$$C_2H_4{}^* \rightleftharpoons C_2H_5-Z \qquad\qquad K_{S1} \qquad\qquad \text{(S18)}$$

$$C_4H_8(g) + C_2H_5-Z \rightleftharpoons C_4H_8-C_2H_5-Z \qquad\qquad K_{C_4H_8-C_2H_5-Z} \qquad\qquad \text{(S19)}$$

$$C_4H_8-C_2H_5-Z \rightarrow C_2H_6-C_4H_6{}^* \qquad\qquad k_{S2} \qquad\qquad \text{(S20)}$$
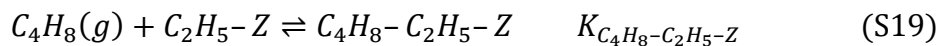
The rate of C_2H_5–Z hydride transfer is given by:

$$r = k_{S2}[C_4H_8 - C_2H_5 - Z] \tag{S21}$$

Combining Eq. S21 with Eqs. S5, S17, S18, and S19 yields:

$$r = K_{C_2H_4}K_{S1}K_{C_4H_8-C_2H_5-Z}k_{S2}(C_2H_4)(C_4H_8)[*] \tag{S22}$$

And normalized by the number of sites [L]:

$$\frac{r}{L} = K_{C_2H_4}K_{C_4H_8-C_2H_5-Z}k_{S2}(C_2H_4)(C_4H_8)\left(\frac{[*]}{[L]}\right) \tag{S23}$$

The concerted mechanism of the alkene-mediated pathway consists of three steps:

$$C_2H_4(g) + * \rightleftharpoons C_2H_4{}^* \qquad\qquad K_{C_2H_4} \tag{S24}$$

$$C_4H_8(g) + C_2H_4{}^* \rightleftharpoons C_4H_8 - C_2H_4{}^* \qquad K_{C_4H_8-C_2H_4} \tag{S25}$$

$$C_4H_8 - C_2H_4{}^* \rightarrow C_2H_6 - C_4H_6{}^* \qquad k_C \tag{S26}$$
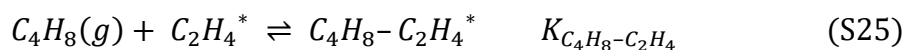
The rate of concerted hydride transfer is given by:

$$r = k_c[C_4H_8 - C_2H_4{}^*] \tag{S27}$$

Combining Eq. S27 with Eqs. S5, S24, and S25 yields:

$$r = K_{C_2H_4}K_{C_4H_8-C_2H_4}k_C(C_2H_4)(C_4H_8)[*] \tag{S28}$$

And normalized by the number of sites [L]:

$$\frac{r}{L} = K_{C_2H_4}K_{C_4H_8-C_2H_4}k_C(C_2H_4)(C_4H_8)\left(\frac{[*]}{[L]}\right) \tag{S29}$$

Potential most abundant surface intermediates (MASI) considered for the CH_2O-mediated pathway considered are [*], CH_3OH^*, CH_3–Z, and $C_4H_8O^*$. The site balance is given by:

$$\frac{[*]}{[L]} = (1 + K_{CH_3OH}(CH_3OH) + K_{CH_3OH}K_{S1}(CH_3OH)(H_2O)^{-1}$$
$$+ K_{CH_3OH}K_{S1}K_{S2}K_3)(CH_3OH)^2(H_2O)^{-1}(C_3H_6) \tag{S30}$$

where K_{S1}, K_{S2}, and K_3, represent rate constants for quasi-equilibrated CH_3–Z formation, CH_2OH–Z formation, and butenol formation.

The first step of the sequential mechanism for the CH_2O-mediated pathway, CH_3–Z formation, involves two steps:

$$CH_3OH(g) + * \rightleftharpoons CH_3OH^* \qquad\qquad K_{CH_3OH} \tag{S31}$$

$$CH_3OH^* \rightarrow H_2O - CH_3\text{-}Z \qquad\qquad k_{CH_3OH} \qquad (S32)$$

The rate is given by:

$$r = k_{S1}[CH_3OH^*] \qquad (S33)$$

Combining Eq. S33 with Eqs. S5 and S3, and normalizing by the number of sites [L] yields:

$$\frac{r}{L} = K_{CH_3OH}k_{S1}(CH_3OH)\frac{[*]}{[L]} \qquad (S34)$$

The second step of the sequential mechanism for the CH$_2$O-mediated pathway, CH$_2$OH–Z formation, involves five steps:

$$CH_3OH(g) + * \rightleftharpoons CH_3OH^* \qquad\qquad K_{CH_3OH} \qquad (S35)$$

$$CH_3OH^* \rightleftharpoons H_2O - CH_3\text{-}Z \qquad\qquad K_{S1} \qquad (S36)$$

$$H_2O - CH_3\text{-}Z \rightleftharpoons CH_3\text{-}Z + H_2O(g) \qquad\qquad \frac{1}{K_{H_2O-CH_3-Z}} \qquad (S37)$$

$$CH_3OH(g) + CH_3\text{-}Z \rightleftharpoons CH_3OH\text{-}CH_3\text{-}Z \qquad\qquad K_{CH_3OH} \qquad (S38)$$

$$CH_3OH\text{-}CH_3\text{-}Z \rightarrow CH_4\text{-}CH_2OH\text{-}Z \qquad\qquad k_{S2} \qquad (S39)$$

The rate is given by:

$$r = k_{S2}[CH_3OH\text{-}CH_3\text{-}Z] \qquad (S40)$$

Combining Eq. S40 with Eqs. S35, S36, S37 and S38, and normalizing by the number of sites [L] yields:

$$\frac{r}{L} = \frac{K_{CH_3OH}{}^2 K_{S1} k_{S2}}{K_{H_2O-CH_3-Z}}(CH_3OH)^2(H_2O)^{-1}\frac{[*]}{[L]} \qquad (S41)$$

The third step of the sequential mechanism for the CH$_2$O-mediated pathway, butenol formation, involves eight steps:

$$CH_3OH(g) + * \rightleftharpoons CH_3OH^* \qquad\qquad K_{CH_3OH} \qquad (S42)$$

$$CH_3OH^* \rightleftharpoons H_2O - CH_3\text{-}Z \qquad\qquad K_{S1} \qquad (S43)$$

$$H_2O - CH_3\text{-}Z \rightleftharpoons CH_3\text{-}Z + H_2O(g) \qquad\qquad \frac{1}{K_{H_2O-CH_3-Z}} \qquad (S44)$$

$$CH_3OH(g) + CH_3\text{-}Z \rightleftharpoons CH_3OH\text{-}CH_3\text{-}Z \qquad\qquad K_{CH_3OH} \qquad (S45)$$

$$CH_3OH\text{-}CH_3\text{-}Z \rightleftharpoons CH_4\text{-}CH_2OH\text{-}Z \qquad\qquad K_{S2} \qquad (S46)$$

$$CH_4-CH_2OH-Z \rightleftharpoons CH_2OH-Z + CH_4(g) \qquad \frac{1}{K_{CH_4-CH_2OH-Z}} \quad (S47)$$

$$C_3H_6(g) + CH_2OH-Z \rightleftharpoons C_3H_6-CH_2OH-Z \qquad K_{C_3H_6-CH_2OH-Z} \quad (S48)$$

$$C_3H_6-CH_2OH-Z \rightarrow C_4H_8O^* \qquad k_3 \quad (S49)$$
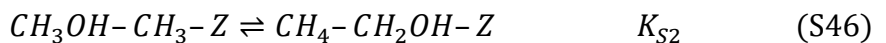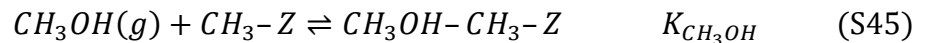
The rate is given by:

$$r = k_3[C_3H_6-CH_2OH-Z] \qquad (S50)$$

Combining Eq. S50 with Eqs. S42, S43, S44, S45, S46, S47, and S48 and normalizing by the number of sites [L] yields:

$$\frac{r}{L} = \frac{K_{CH_3OH}{}^2 K_{S1} K_{S2} k_{S3}}{K_{H_2O-CH_3-Z} K_{CH_4-CH_2OH-Z}} (CH_3OH)^2 (H_2O)^{-1} (CH_4)^{-1} (C_3H_6) \frac{[*]}{[L]} \qquad (S51)$$

The fourth step of the sequential mechanism for the CH$_2$O-mediated pathway, butenol dehydration, involves the same eight steps as butenol formation; however, butenol formation is assumed to be quasi-equilibrated and represented by K$_3$. The additional step, butenol dehydration, is given by Eq. S52:

$$C_4H_8O^* \rightarrow H_2O-C_4H_6{}^* \qquad k_4 \quad (S52)$$

The rate is given by:

$$r = k_4[C_4H_8O^*] \qquad (S53)$$

Combining Eq. S52 with Eqs. S42, S43, S44, S45, S46, S47, S48, and S49 and normalizing by the number of sites [L] yields:

$$\frac{r}{L} = \frac{K_{CH_3OH}{}^2 K_{S1} K_{S2} K_{S3} k_{S4}}{K_{H_2O-CH_3-Z} K_{CH_4-CH_2OH-Z}} (CH_3OH)^2 (H_2O)^{-1} (CH_4)^{-1} (C_3H_6) \frac{[*]}{[L]} \qquad (S54)$$

The concerted CH$_2$O formation step involves three steps:

$$CH_3OH(g) + * \rightleftharpoons CH_3OH^* \qquad K_{CH_3OH} \quad (S55)$$

$$CH_3OH(g) + CH_3OH^* \rightleftharpoons 2CH_3OH^* \qquad K_{2CH_3OH} \quad (S56)$$

$$2CH_3OH^* \rightarrow CH_4-H_2O-CH_2O \qquad k_C \quad (S57)$$
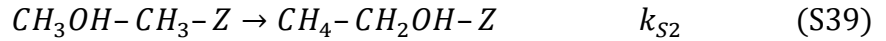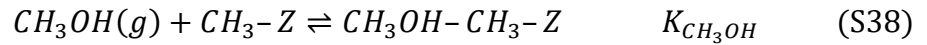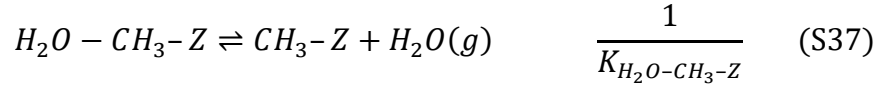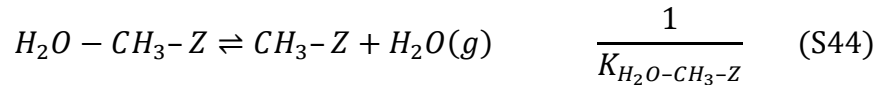
The rate is given by:
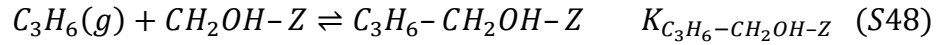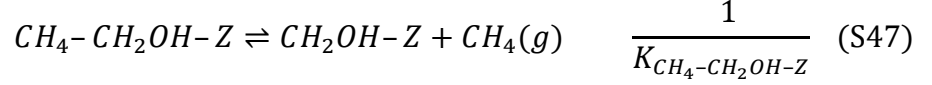
$$r = k_C[2CH_3OH^*] \qquad (S58)$$

Combining Eq. S58 with Eqs. S5, S55, S56, and S57 and normalizing by the number of sites [L] yields:

$$r = K_{CH_3OH}K_{2CH_3OH}k_C(CH_3OH)^2 \qquad (S59)$$

CH_2O protonation involves five steps:

$$CH_3OH(g) + * \rightleftharpoons CH_3OH^* \qquad\qquad K_{CH_3OH} \qquad (S60)$$

$$CH_3OH(g) + CH_3OH^* \rightleftharpoons 2CH_3OH^* \qquad\qquad K_{2CH_3OH} \qquad (S61)$$

$$2CH_3OH^* \rightleftharpoons CH_4 - H_2O - CH_2O \qquad\qquad K_C \qquad (S62)$$

$$CH_4 - H_2O - CH_2O \rightleftharpoons CH_2O^* + CH_4(g) + H_2O(g) \qquad \frac{1}{K_{H_2O}K_{CH_4}} \qquad (S63)$$
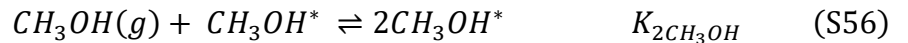
$$CH_2O^* \rightarrow CH_2OH - Z \qquad\qquad k_5 \qquad (S64)$$
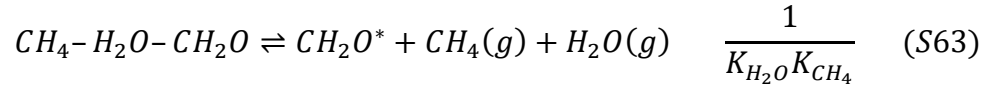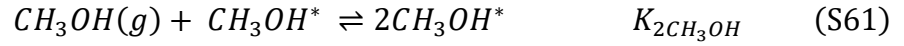
The rate is given by:

$$r = k_5[CH_2O^*] \qquad (S65)$$

Combining Eq. S65 with Eqs. S5, S60, S61, S62, and S63 and normalizing by the number of sites [L] yields:

$$r = \frac{K_{CH_3OH}K_{2CH_3OH}K_Ck_5}{K_{H_2O}K_{CH_4}}(CH_3OH)^2(H_2O)^{-1}(CH_4)^{-1} \qquad (S66)$$

S4. Images of Alkene-mediated Reactions in MFI at each O-site

	O14-O25	O16-O14	O16-O25
ΔG	21	25	0

Figure S3. C_2H_5–Z formation transition state at a) O14-O25, b) O16-O14, and c) O16-O25. Free energies (ΔG, kJ mol^{-1}) are reported at 433 K and are relative to the transition state at the most favorable O-site. The most favorable transition state has a ΔG of 0 kJ mol^{-1} and is used for further analysis.

Figure S4. C_2H_5–Z formation with spectating C_4H_8 transition state at a) O14-O25, b) O16-O14, and c) O16-O25. Free energies (ΔG, kJ mol^{-1}) are reported at 433 K and are relative to the transition state at the most favorable O-site. The most favorable transition state has a ΔG of 0 kJ mol^{-1} and is used for further analysis.
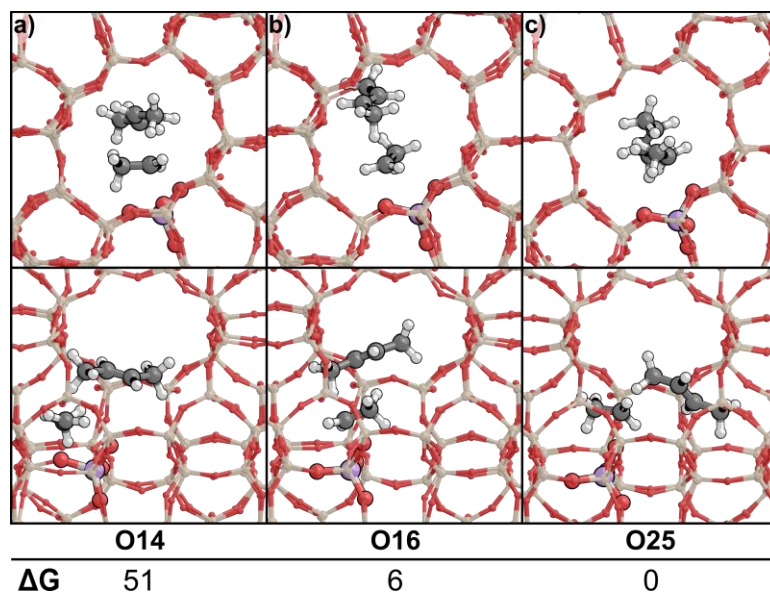
Figure S5. C_2H_5–Z hydride transfer transition state at a) O14, b) O16, and c) O25. Free energies (ΔG, kJ mol^{-1}) are reported at 433 K and are relative to the transition state at the most favorable O-site. The most favorable transition state has a ΔG of 0 kJ mol^{-1} and is used for further analysis.

	O14	O16	O25
ΔG	30	39	0

Figure S6. Concerted hydride transfer transition state at a) O14, b) O16, and c) O25. Free energies (ΔG, kJ mol^{-1}) are reported at 433 K and are relative to the transition state at the most favorable O-site. The most favorable transition state has a ΔG of 0 kJ mol^{-1} and is used for further analysis.

S5. Images of Alkene-mediated Reactions in CHA at Each O-site

	O1-O2	O1-O3	O2-O3	O2-O4
ΔG	9	0	10	31
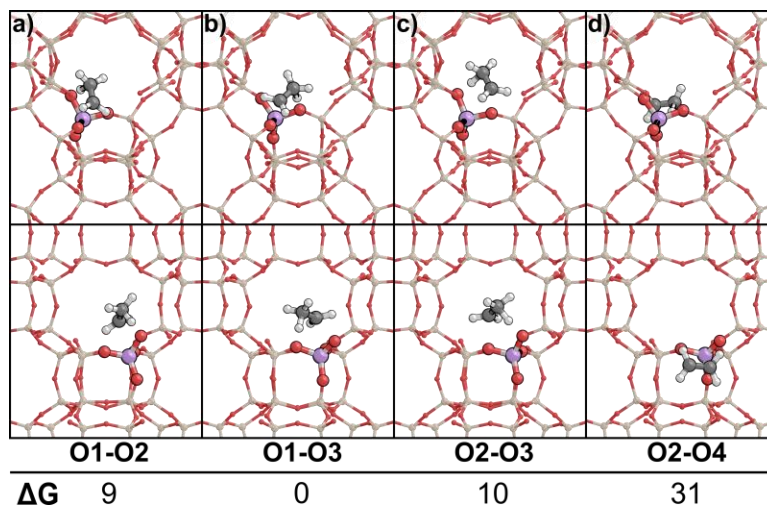
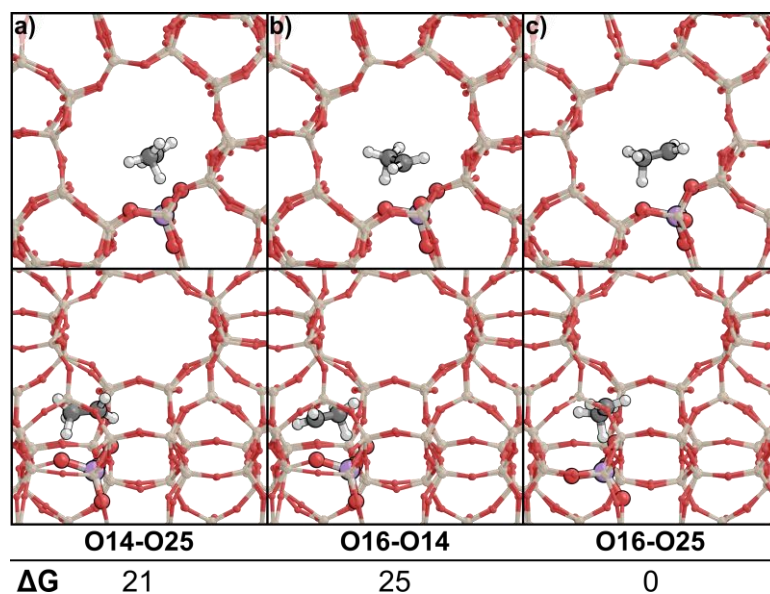**Figure S7.** C_2H_5–Z formation transition state at a) O1, b) O2, c) O3, and d) O4. Free energies (ΔG, kJ mol^{-1}) are reported at 433 K and are relative to the transition state at the most favorable O-site. The most favorable transition state has a ΔG of 0 kJ mol^{-1} and is used for further analysis.
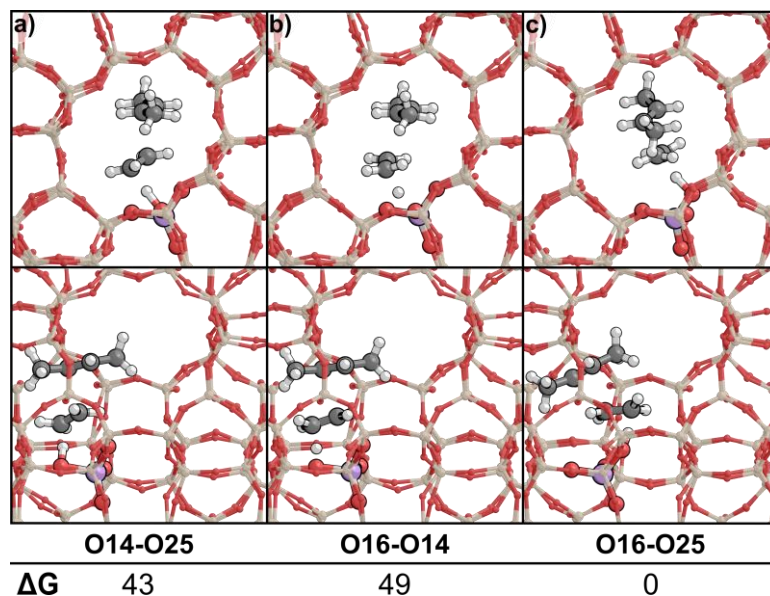
Figure S8. C_2H_5–Z hydride transfer transition state at a) O1, b) O3, and c) O4. Free energies (ΔG, kJ mol^{-1}) are reported at 433 K and are relative to the transition state at the most favorable O-site. The most favorable transition state has a ΔG of 0 kJ mol^{-1} and is used for further analysis.

Figure S9. Concerted hydride transfer transition state at a) O1, b) O2, and c) O3. Free energies (ΔG, kJ mol^{-1}) are reported at 433 K and are relative to the transition state at the most favorable O-site. The most favorable transition state has a ΔG of 0 kJ mol^{-1} and is used for further analysis.

S6. Images of CH₂O-mediated Reactions in MFI at Each O-site

	O14	**O16**	**O25**
ΔG	38	11	0
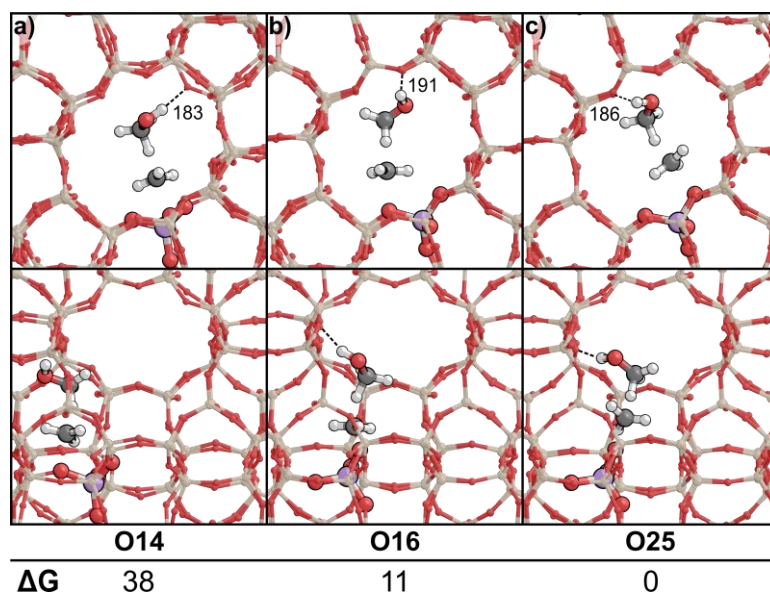
Figure S10. CH$_2$OH–Z formation transition state at a) O14, b) O16, and c) O25. Free energies (ΔG, kJ mol^{-1}) are reported at 433 K and are relative to the transition state at the most favorable O-site. The most favorable transition state has a ΔG of 0 kJ mol^{-1} and is used for further analysis.

S7. Images of CH₂O-mediated Reactions in CHA at Each O-site

	O1	**O2**	**O3**	**O4**
ΔG	6	7	1	0
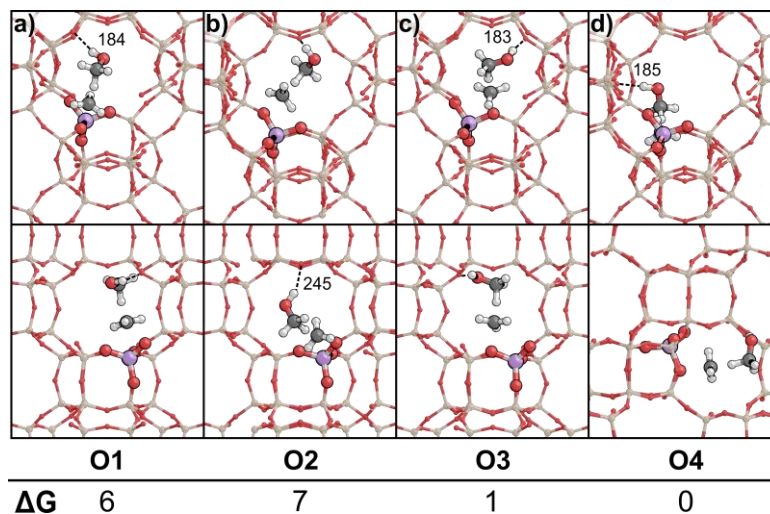
Figure S11. CH$_2$OH–Z formation transition state at a) O1, b) O2, c) O3, and d) O4. Free energies (ΔG, kJ mol^{-1}) are reported at 433 K and are relative to the transition state at the most favorable O-site. The most favorable transition state has a ΔG of 0 kJ mol^{-1} and is used for further analysis
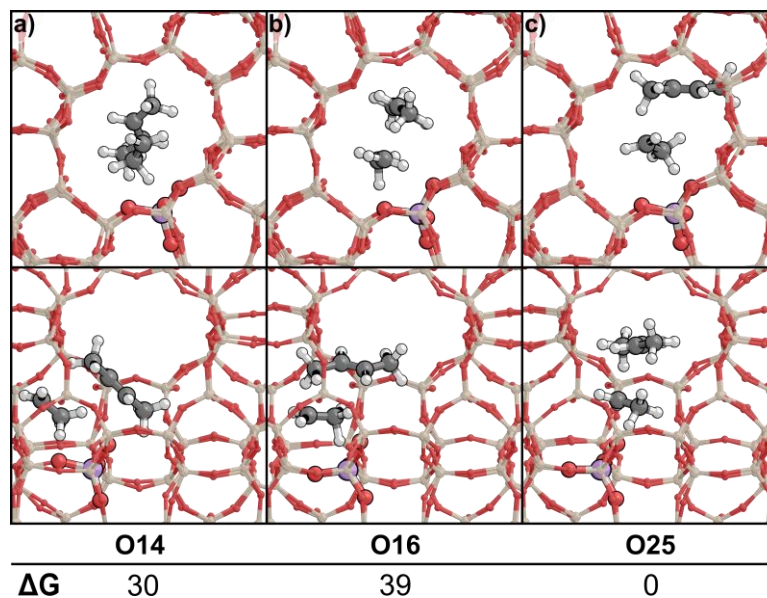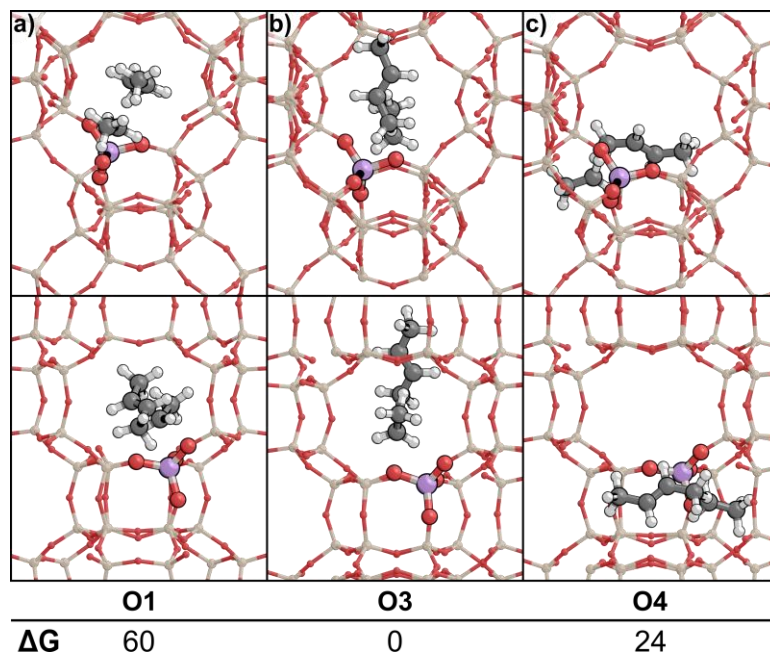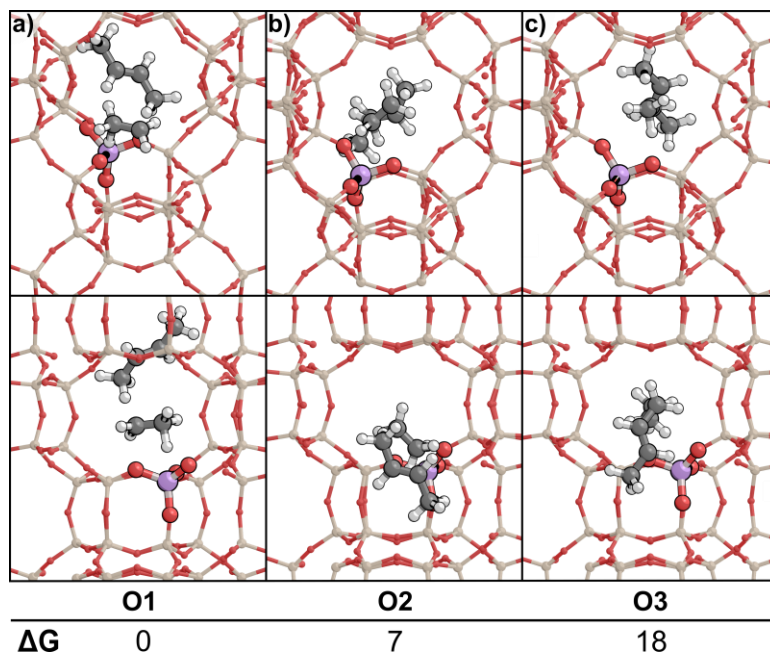
S8. Energies of Hydride Transfer Transition States with C₁-C₄ Alkyls

Table S1. $\Delta\Delta Ga^{\neq}$ (kJ mol^{-1}) values for each surface-bound alkyl in MFI and CHA. Values are reported at 623 K

Surface-bound Alkyl	$\Delta\Delta Ga^{\neq}$ kJ mol^{-1}	
	MFI	*CHA*
Methyl	19	17
Ethyl	13	34
Propyl	21	3
Sec-butyl	2	18
Tert-butyl	-101	-89

Table S2. $\Delta Ga^{\neq}$ (kJ mol^{-1}) for hydride transfers between each surface-bound alkyl and C₄H₈ or CH₃OH. Values are reported at 623 K.

Hydride Transfer Transition State	$\Delta Ga^{\neq}$ kJ mol^{-1}	
	MFI	*CHA*
[Methyl--CH₃OH]$^{\neq}$	156	160
[Ethyl--CH₃OH]$^{\neq}$	147	149
[Propyl--CH₃OH]$^{\neq}$	104	108
[Sec-butyl--CH₃OH]$^{\neq}$	100	113
[Tert-butyl--CH₃OH]$^{\neq}$	55	104
[Methyl--C₄H₈]$^{\neq}$	137	143
[Ethyl--C₄H₈]$^{\neq}$	134	115
[Propyl--C₄H₈]$^{\neq}$	83	106
[Sec-butyl--C₄H₈]$^{\neq}$	98	96
[Tert-butyl--C₄H₈]$^{\neq}$	156	192

Figure S12. Transition state of hydride transfer between CH$_3$OH and a) methyl, b) ethyl, c) propyl, d) sec-butyl, and e) tert-butyl in MFI.
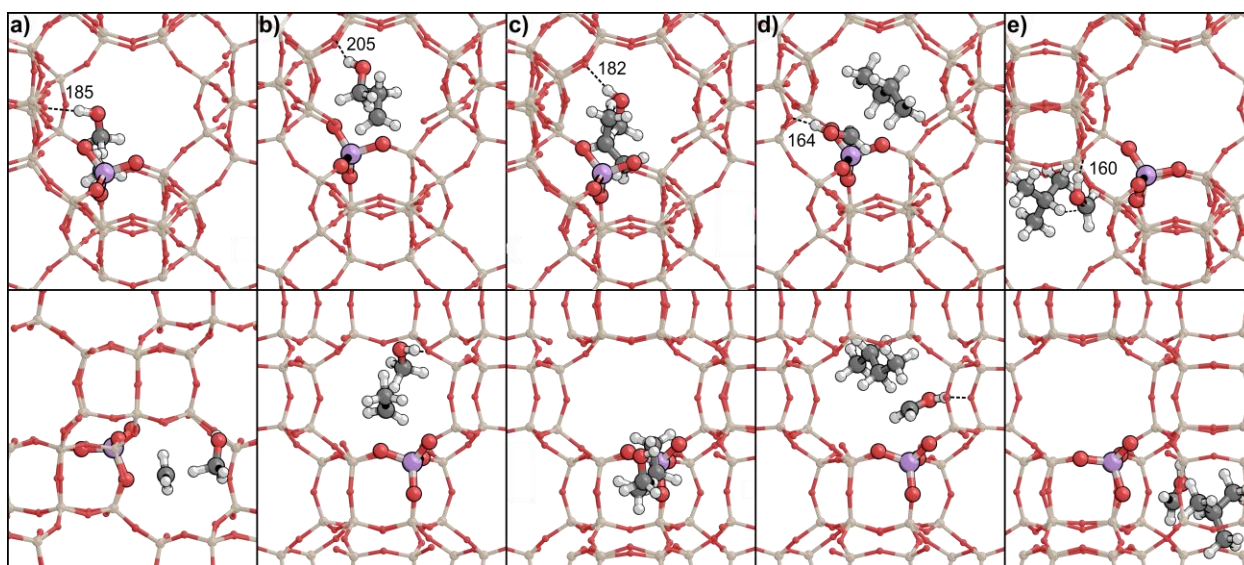
Figure S13. Transition state of hydride transfer between CH$_3$OH and a) methyl, b) ethyl, c) propyl, d) sec-butyl, and e) tert-butyl in CHA.
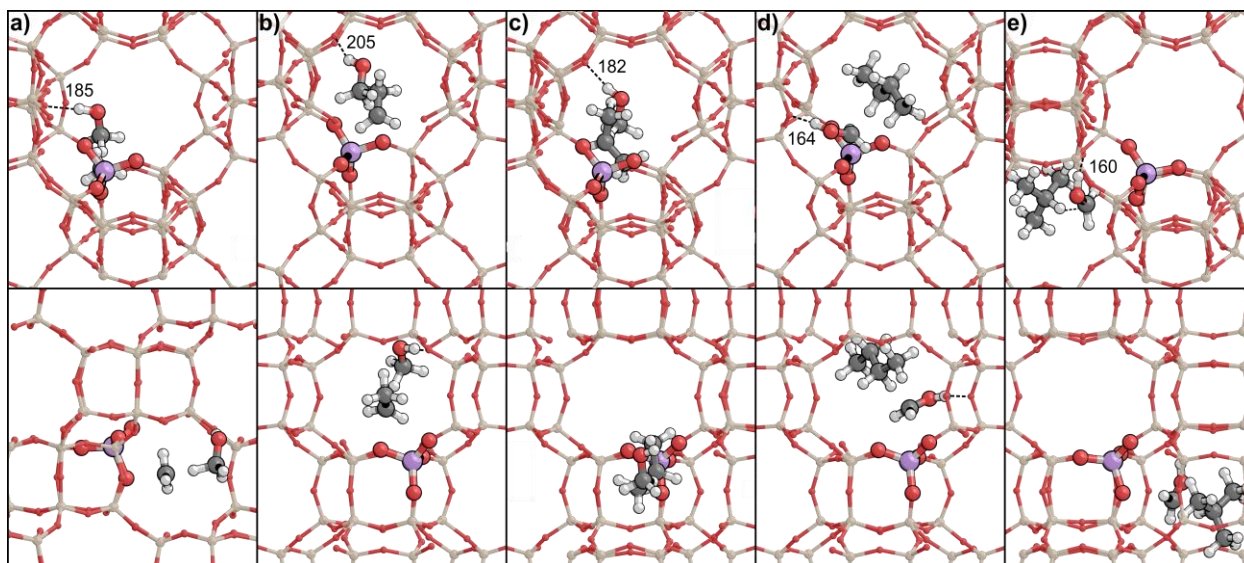
Figure S14. Transition state of hydride transfer between C_4H_8 and a) methyl, b) ethyl, c) propyl, d) sec-butyl, and e) tert-butyl in MFI.
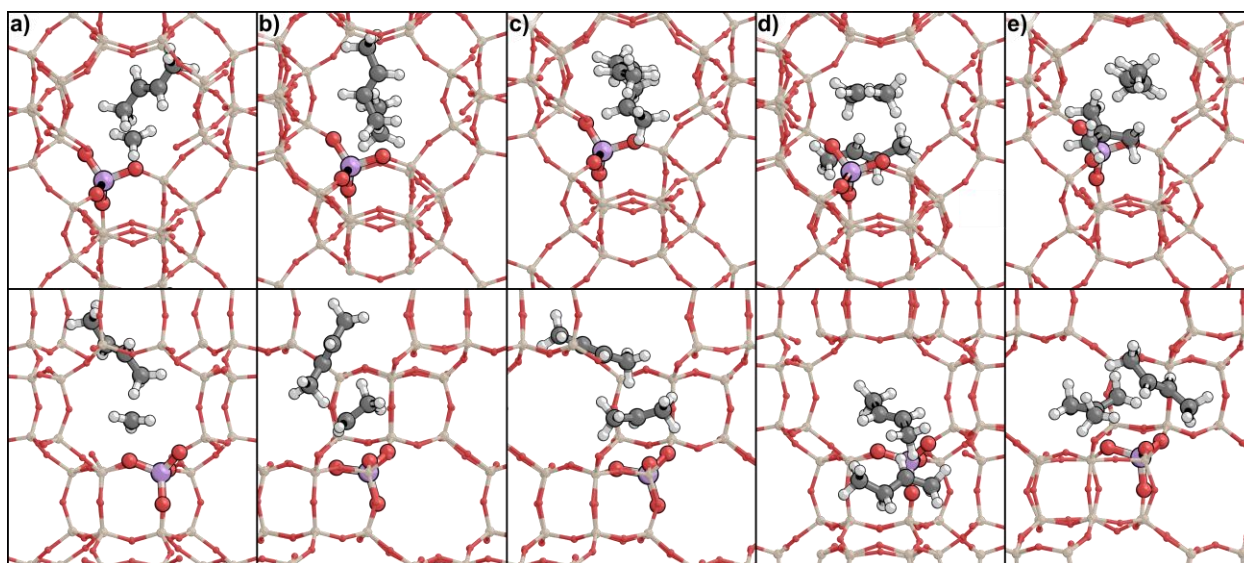
Figure S15. Transition state of hydride transfer between C_4H_8 and a) methyl, b) ethyl, c) propyl, d) sec-butyl, and e) tert-butyl in CHA.

S10. Images of Reaction Coordinate Diagram States

	[C₂H₄--H−Z]		[TS]‡		[C₂H₅−Z]
ΔH	−50	*(68)*	18	*(−30)*	−80
ΔS	−127	*(−34)*	−161	*(−29)*	−156
ΔG	5	*(83)*	88	*(−18)*	−13

Figure S16. C_2H_5–Z formation a) reactant, b) transition state, and c) product in MFI. Enthalpy (ΔH), entropy (ΔS), and free energy (ΔG) values are reported at 433 K and relative to a protonated zeolite. Intrinsic barriers (ΔE_{act}) and overall barriers (ΔE_{rxn}) are listed in italics.

	[C4H8--C₂H₄--H−Z]		[TS]‡		[C4H8--C₂H₅−Z]
ΔH	−81	*(63)*	−18	*(−33)*	−114
ΔS	−287	*(−45)*	−332	*(−37)*	−324
ΔG	43	*(83)*	126	*(−16)*	27

Figure S17. C_2H_5–Z formation with spectating C_4H_8 a) reactant, b) transition state, and c) product in MFI. Enthalpy (ΔH), entropy (ΔS), and free energy (ΔG) values are reported at 433 K and relative to a protonated zeolite. Intrinsic barriers (ΔE_{act}) and overall barriers (ΔE_{rxn}) are listed in italics.

	[C₄H₈--C₂H₅−Z]		[TS]‡		[C₂H₆--C₄H₆--H−Z]
ΔH	−114	*(70)*	−44	*(−10)*	−124
ΔS	−324	*(21)*	−303	*(55)*	−269
ΔG	27	*(61)*	88	*(−34)*	−7

Figure S18. C_2H_5–Z hydride transfer a) reactant, b) transition state, and c) product in MFI. Enthalpy (ΔH), entropy (ΔS), and free energy (ΔG) values are reported at 433 K and relative to a protonated zeolite. Intrinsic barriers (ΔE_{act}) and overall barriers (ΔE_{rxn}) are listed in italics.

	[C₄H₈--C₂H₄−Z]		[TS]‡		[C₂H₆--C₄H₆--H−Z]
ΔH	−81	*(43)*	−38	*(−43)*	−124
ΔS	−287	*(−28)*	−315	*(18)*	−269
ΔG	43	*(55)*	98	*(−50)*	−7

Figure S19. Concerted hydride transfer a) reactant, b) transition state, and c) product in MFI. Enthalpy (ΔH), entropy (ΔS), and free energy (ΔG) values are reported at 433 K and relative to a protonated zeolite. Intrinsic barriers (ΔE_{act}) and overall barriers (ΔE_{rxn}) are listed in italics.

	[C$_2$H$_4$--H−Z]		[TS]‡		[C$_2$H$_5$−Z]
ΔH	−63	*(72)*	9	*(−27)*	−90
ΔS	−140	*(−33)*	−173	*(−29)*	−169
ΔG	−3	*(86)*	83	*(−14)*	−17

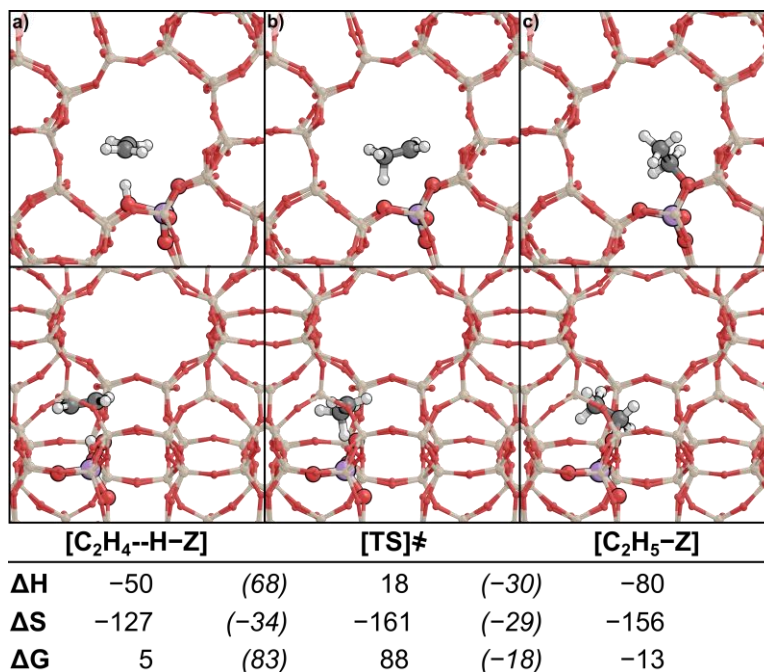**Figure S20.** C$_2$H$_5$–Z formation a) reactant, b) transition state, and c) product in CHA. Enthalpy (ΔH), entropy (ΔS), and free energy (ΔG) values are reported at 433 K and relative to a protonated zeolite. Intrinsic barriers (ΔE$_{act}$) and overall barriers (ΔE$_{rxn}$) are listed in italics.

[C4H8--C2H4--H−Z]		[TS]‡		[C4H8--C2H5−Z]
ΔH	−105	*(67)*	−38	*(−34)*	−139
ΔS	−274	*(−38)*	−312	*(−42)*	−316
ΔG	13	*(84)*	97	*(−16)*	−3

Figure S21. C_2H_5–Z formation with spectating C_4H_8 a) reactant, b) transition state, and c) product in CHA. Enthalpy (ΔH), entropy (ΔS), and free energy (ΔG) values are reported at 433 K and relative to a protonated zeolite. Intrinsic barriers (ΔE_{act}) and overall barriers (ΔE_{rxn}) are in italics.

	[C$_4$H$_8$--C$_2$H$_5$−Z]		[TS]$\neq$		[C$_2$H$_6$--C$_4$H$_6$--H−Z]
ΔH	−139	*(74)*	−65	*(8)*	−131
ΔS	−316	*(−9)*	−325	*(54)*	−262
ΔG	−3	*(78)*	75	*(−14)*	−17

Figure S22. C$_2$H$_5$–Z hydride transfer a) reactant, b) transition state, and c) product in CHA. Enthalpy (ΔH), entropy (ΔS), and free energy (ΔG) values are reported at 433 K and relative to a protonated zeolite. Intrinsic barriers (ΔE$_{act}$) and overall barriers (ΔE$_{rxn}$) are listed in italics.
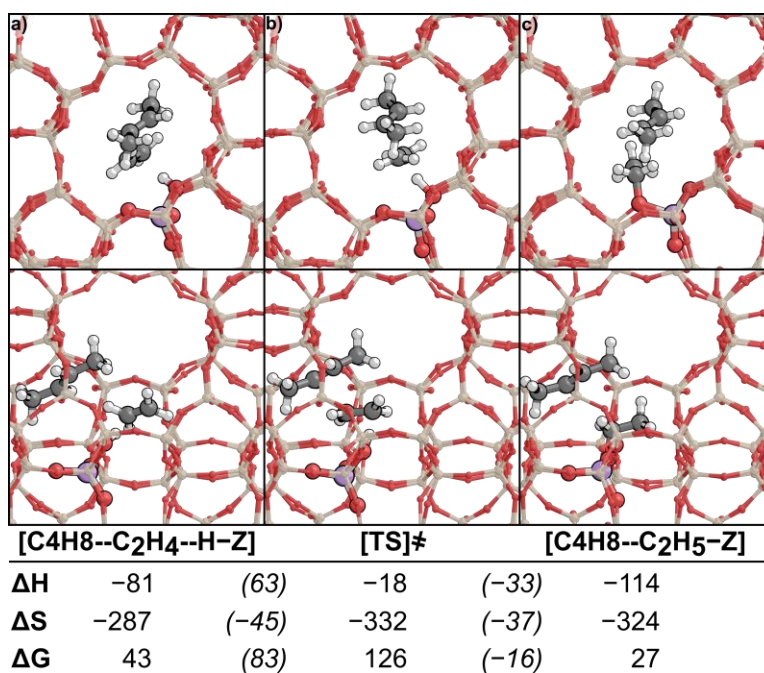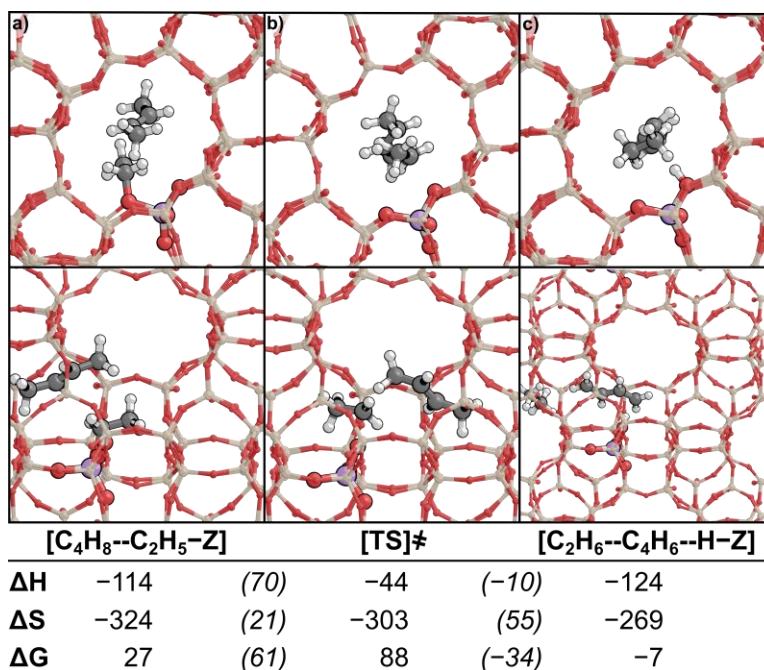
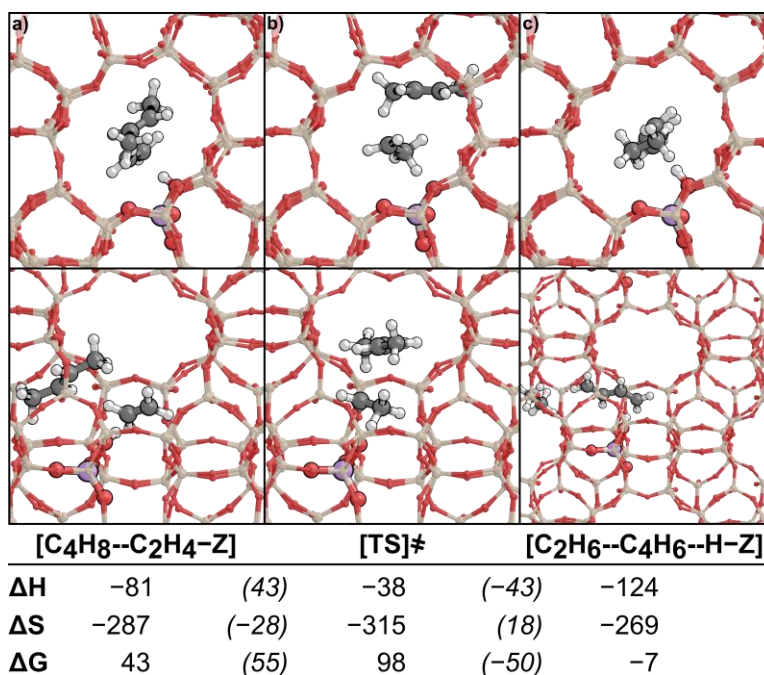| [C4H8--C_2H_4--H–Z]			[TS]$^{\neq}$		[C_2H_6--C_4H_6--H–Z]
ΔH	−105	*(55)*	−50	*(−26)*	−131
ΔS	−274	*(−43)*	−317	*(12)*	−262
ΔG	13	*(74)*	87	*(−30)*	−17

Figure S23. Concerted hydride transfer a) reactant, b) transition state, and c) product in MFI. Enthalpy (ΔH), entropy (ΔS), and free energy (ΔG) values are reported at 433 K and relative to a protonated zeolite. Intrinsic barriers (ΔE$_{act}$) and overall barriers (ΔE$_{rxn}$) are listed in italics.

[CH_3OH--H–Z]			[TS]$^{\neq}$		[H_2O--CH_3–Z]
ΔH	−82	*(119)*	37	*(56)*	−26
ΔS	−147	*(−22)*	−169	*(20)*	−127
ΔG	−19	*(129)*	110	*(49)*	30

Figure S24. CH_3–Z formation a) reactant, b) transition state, and c) product in MFI. Enthalpy (ΔH), entropy (ΔS), and free energy (ΔG) values are reported at 433 K and relative to a protonated zeolite. Intrinsic barriers (ΔE$_{act}$) and overall barriers (ΔE$_{rxn}$) are listed in italics.
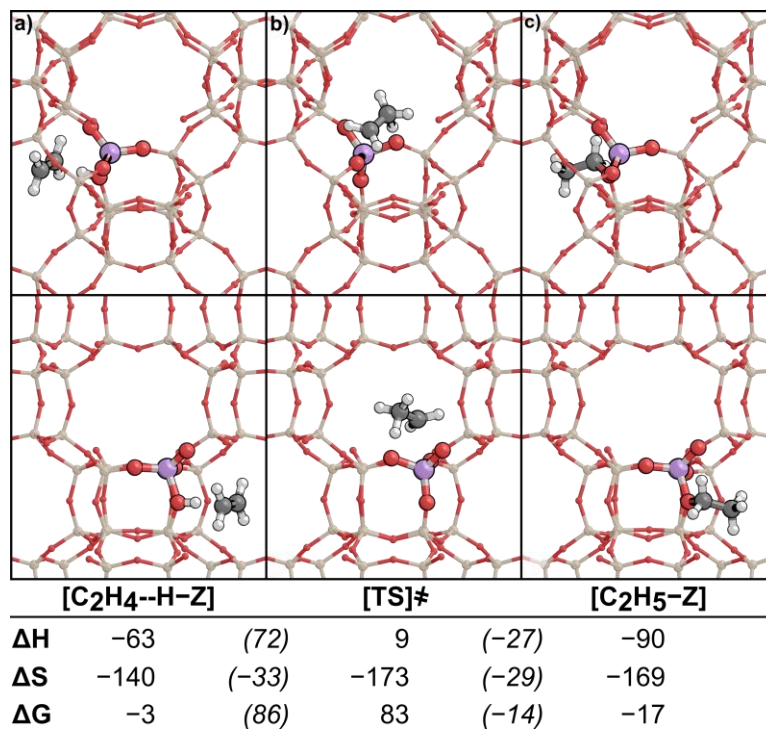
	[CH$_3$OH--CH$_3$–Z]		[TS]$\neq$		[CH$_4$--CH$_2$OH–Z]
ΔH	−33	*(83)*	50	*(−52)*	−85
ΔS	−133	*(−44)*	−177	*(−8)*	−141
ΔG	25	*(102)*	127	*(−49)*	−24

Figure S25. CH$_2$OH–Z formation a) reactant, b) transition state, and c) product in MFI. Enthalpy (ΔH), entropy (ΔS), and free energy (ΔG) values are reported at 433 K and relative to a protonated zeolite. Intrinsic barriers (ΔE$_{act}$) and overall barriers (ΔE$_{rxn}$) are listed in italics.
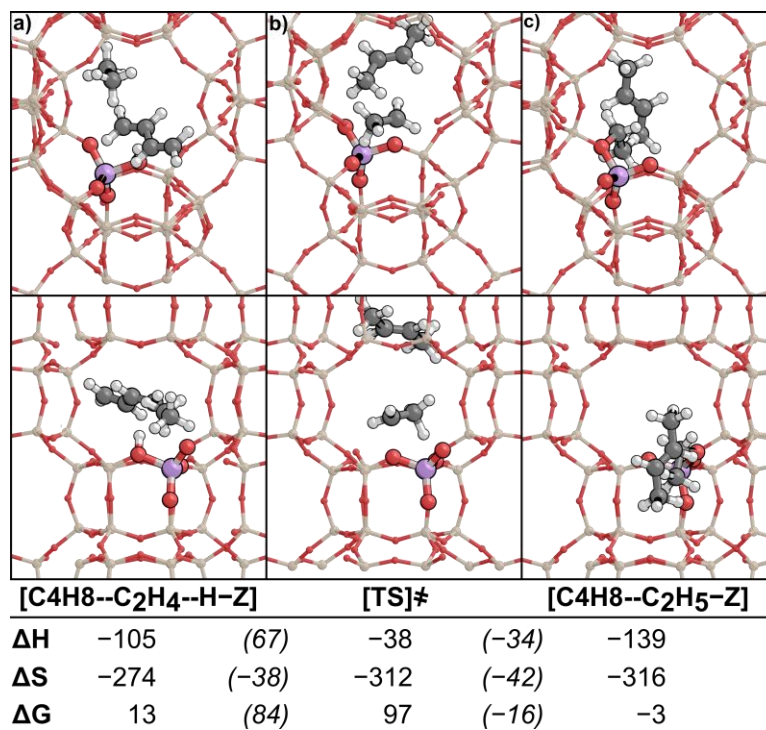

	[2CH$_3$OH--H−Z]		[TS]$\neq$		[H$_2$O--CH$_4$--CH$_2$O--H−Z]
ΔH	−141	*(156)*	15	*(31)*	−110
ΔS	−285	*(−15)*	−300	*(82)*	−203
ΔG	−17	*(162)*	145	*(−6)*	−23

Figure S26. Concerted CH$_2$O formation a) reactant, b) transition state, and c) product in MFI. Enthalpy (ΔH), entropy (ΔS), and free energy (ΔG) values are reported at 433 K and relative to a protonated zeolite. Intrinsic barriers (ΔE$_{act}$) and overall barriers (ΔE$_{rxn}$) are listed in italics.
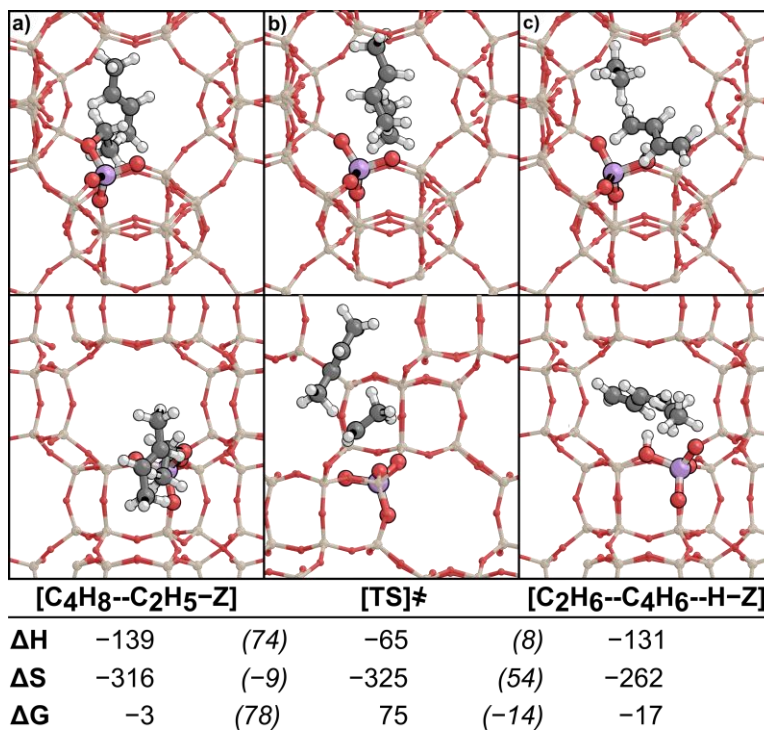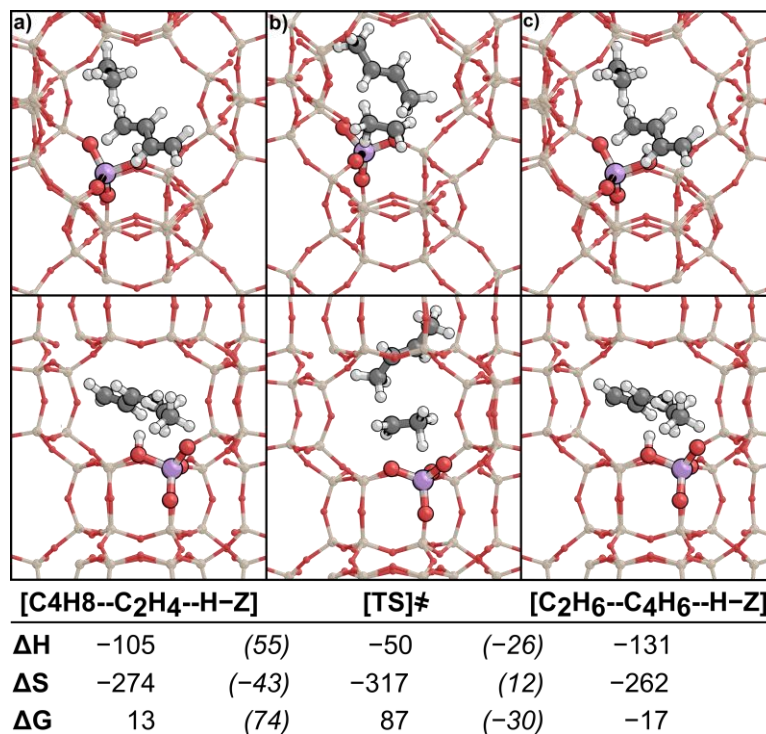
	[CH₂O--H−Z]		[TS]‡		[CH₂OH−Z]
ΔH	−77	*(51)*	−26	*(11)*	−66
ΔS	−16	*(−42)*	−58	*(−31)*	−47
ΔG	−70	*(69)*	−1	*(25)*	−45

Figure S27. CH₂O protonation a) reactant, b) transition state, and c) product in MFI. Enthalpy (ΔH), entropy (ΔS), and free energy (ΔG) values are reported at 433 K and relative to a protonated zeolite. Intrinsic barriers (ΔE$_{act}$) and overall barriers (ΔE$_{rxn}$) are listed in italics.
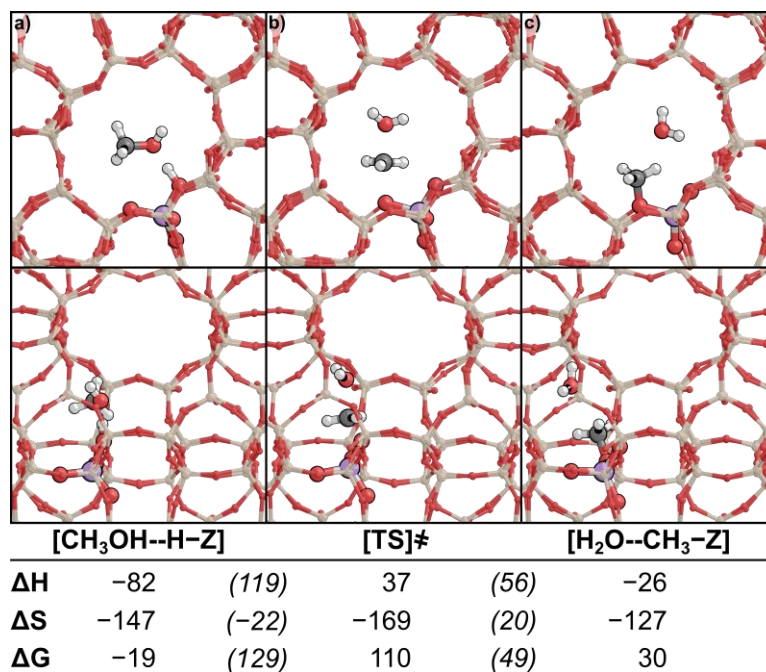

	[C₃H₆--CH₂OH−Z]		[TS]‡		[C₄H₇OH--H−Z]
ΔH	−121	*(34)*	−87	*(−99)*	−220
ΔS	−194	*(6)*	−188	*(−13)*	−207
ΔG	−37	*(32)*	−5	*(−93)*	−130

Figure S28. Butenol formation a) reactant, b) transition state, and c) product in MFI. Enthalpy (ΔH), entropy (ΔS), and free energy (ΔG) values are reported at 433 K and relative to a protonated zeolite. Intrinsic barriers (ΔE$_{act}$) and overall barriers (ΔE$_{rxn}$) are listed in italics.
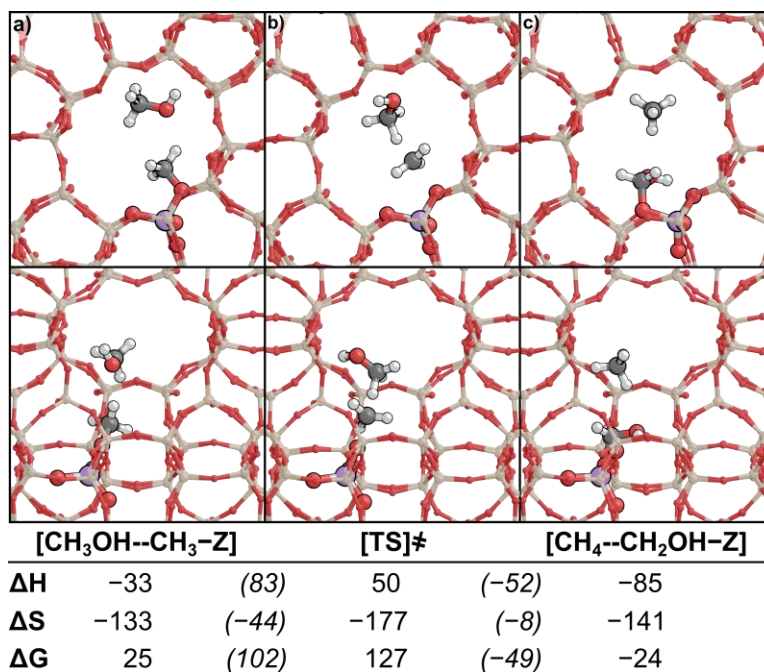
	[C₄H₇OH--H−Z]		[TS]‡		[H₂O--C₄H₆--H−Z]
ΔH	−220	*(90)*	−130	*(75)*	−145
ΔS	−207	*(26)*	−181	*(61)*	−146
ΔG	−130	*(79)*	−51	*(48)*	−82

Figure S29. Butenol dehydration a) reactant, b) transition state, and c) product in MFI. Enthalpy (ΔH), entropy (ΔS), and free energy (ΔG) values are reported at 433 K and relative to a protonated zeolite. Intrinsic barriers (ΔE$_{act}$) and overall barriers (ΔE$_{rxn}$) are listed in italics.
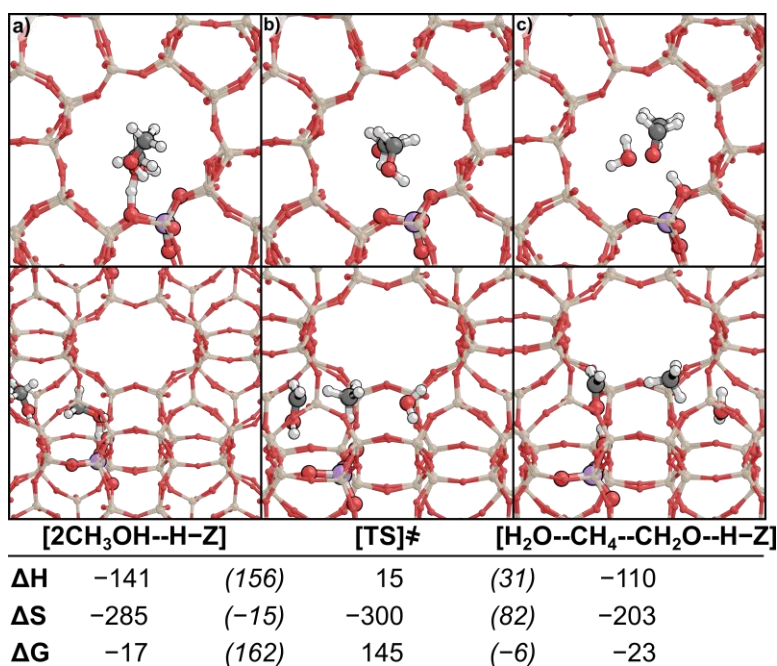

	[CH₃OH--H−Z]		[TS]‡		[H₂O--CH₃−Z]
ΔH	−116	*(126)*	10	*(77)*	−39
ΔS	−167	*(−9)*	−176	*(43)*	−124
ΔG	−44	*(130)*	86	*(59)*	15

Figure S30. CH₃–Z formation a) reactant, b) transition state, and c) product in CHA. Enthalpy (ΔH), entropy (ΔS), and free energy (ΔG) values are reported at 433 K and relative to a protonated zeolite. Intrinsic barriers (ΔE$_{act}$) and overall barriers (ΔE$_{rxn}$) are listed in italics.
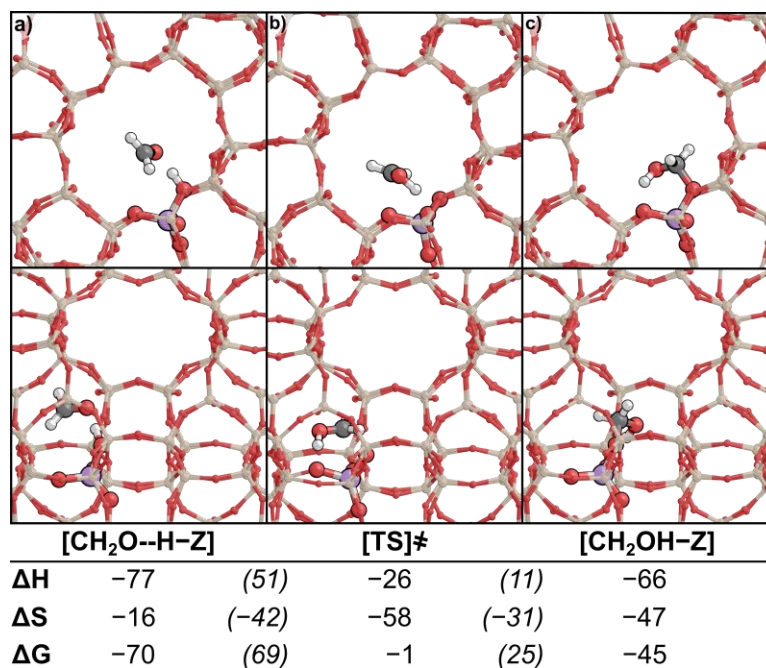
	[CH$_3$OH--CH$_3$−Z]		[TS]‡		[CH$_4$--CH$_2$OH−Z]
ΔH	−50	*(85)*	35	*(−51)*	−101
ΔS	−154	*(−35)*	−189	*(15)*	−139
ΔG	16	*(101)*	117	*(−57)*	−41

Figure S31. CH$_2$OH–Z formation a) reactant, b) transition state, and c) product in CHA. Enthalpy (ΔH), entropy (ΔS), and free energy (ΔG) values are reported at 433 K and relative to a protonated zeolite. Intrinsic barriers (ΔE$_{act}$) and overall barriers (ΔE$_{rxn}$) are listed in italics.
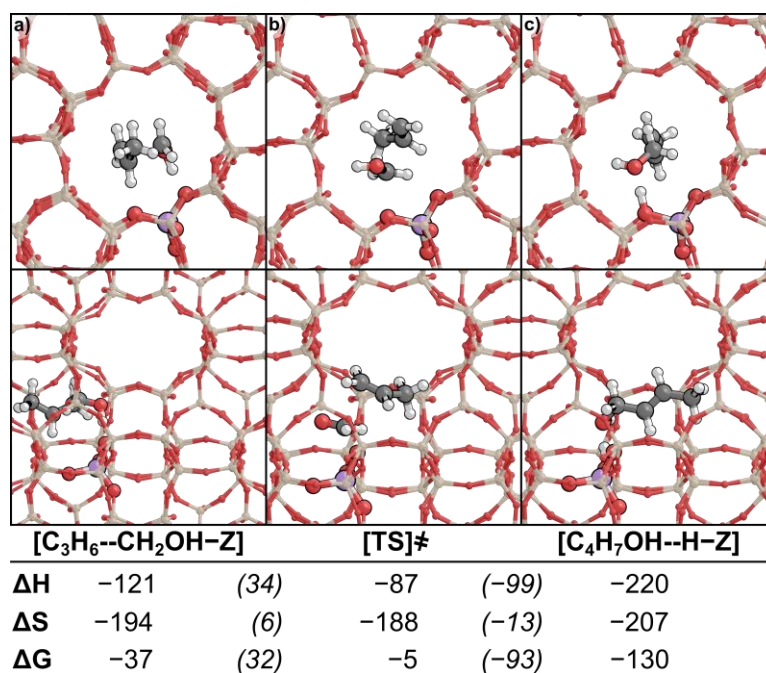
	[2CH₃OH--H−Z]		[TS]≠		[H₂O--CH₄--CH₂O--H−Z]
ΔH	−150	*(121)*	−29	*(16)*	−134
ΔS	−280	*(−49)*	−329	*(60)*	−220
ΔG	−29	*(143)*	114	*(−10)*	−39

Figure S32. Concerted CH₂O formation a) reactant, b) transition state, and c) product in CHA. Enthalpy (ΔH), entropy (ΔS), and free energy (ΔG) values are reported at 433 K and relative to a protonated zeolite. Intrinsic barriers (ΔE$_{act}$) and overall barriers (ΔE$_{rxn}$) are listed in italics.
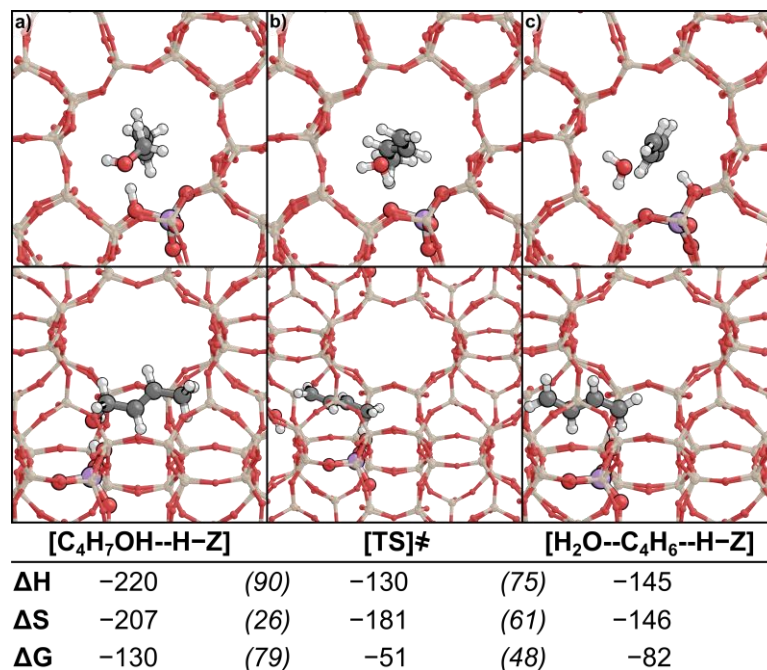
	[CH$_2$O--H−Z]		[TS]$\ddagger$		[CH$_2$OH−Z]
ΔH	−89	*(41)*	−48	*(38)*	−51
ΔS	−23	*(−51)*	−74	*(−39)*	−62
ΔG	−79	*(64)*	−15	*(55)*	−24

Figure S33. CH$_2$O protonation a) reactant, b) transition state, and c) product in CHA. Enthalpy (ΔH), entropy (ΔS), and free energy (ΔG) values are reported at 433 K and relative to a protonated zeolite. Intrinsic barriers (ΔE$_{act}$) and overall barriers (ΔE$_{rxn}$) are listed in italics.
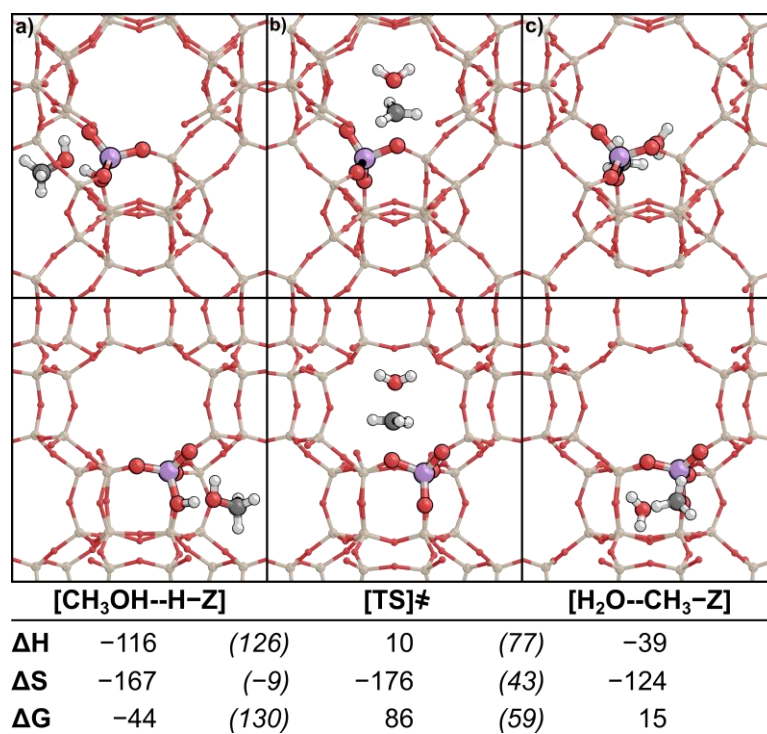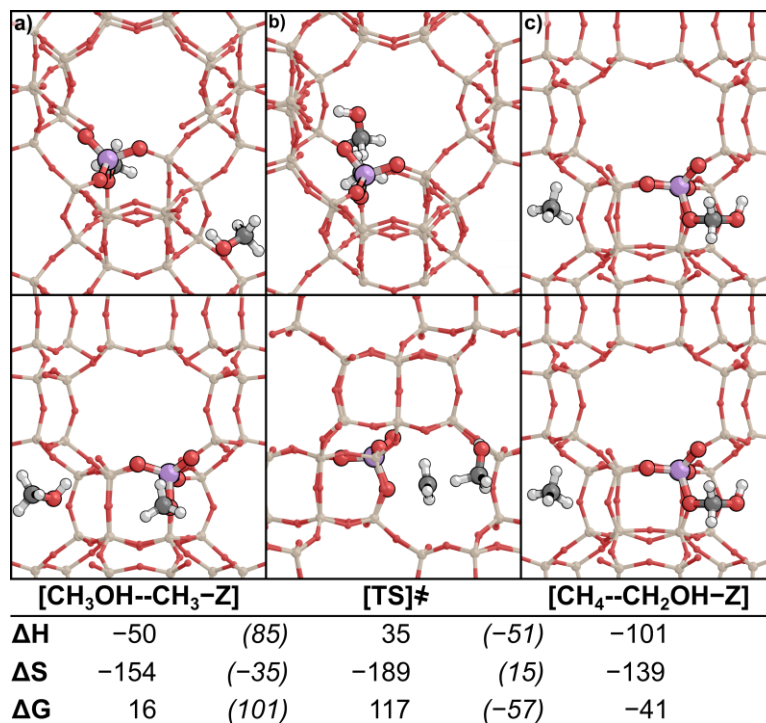
	[C$_3$H$_6$--CH$_2$OH−Z]		[TS]$\neq$		[C$_4$H$_7$OH--H−Z]
ΔH	−129	*(11)*	−118	*(−116)*	−245
ΔS	−178	*(−24)*	−202	*(−41)*	−219
ΔG	−52	*(21)*	−31	*(−98)*	−150

Figure S34. Butenol formation a) reactant, b) transition state, and c) product in CHA. Enthalpy (ΔH), entropy (ΔS), and free energy (ΔG) values are reported at 433 K and relative to a protonated zeolite. Intrinsic barriers (ΔE$_{act}$) and overall barriers (ΔE$_{rxn}$) are listed in italics.
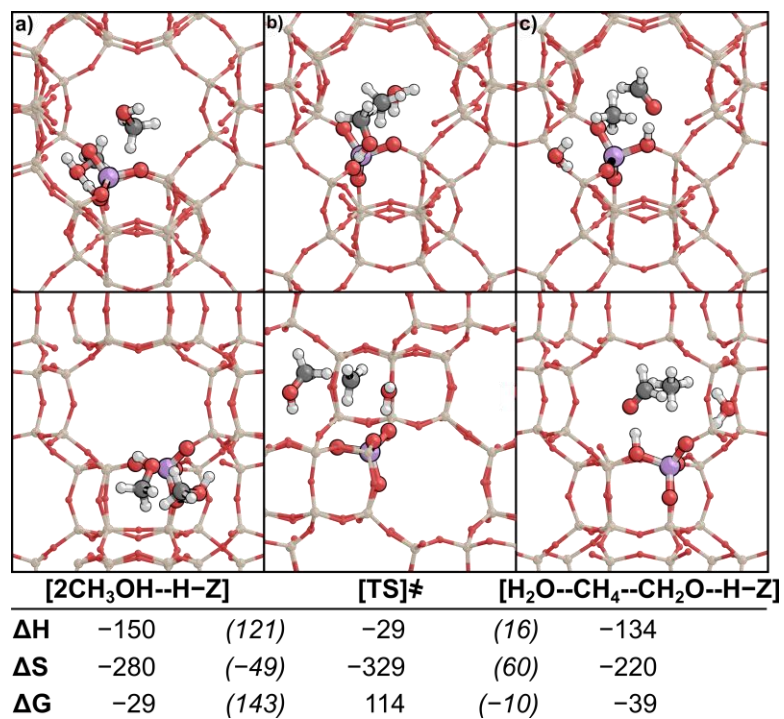
Figure S35. Butenol dehydration a) reactant, b) transition state, and c) product in CHA. Enthalpy (ΔH), entropy (ΔS), and free energy (ΔG) values are reported at 433 K and relative to a protonated zeolite. Intrinsic barriers (ΔE$_{act}$) and overall barriers (ΔE$_{rxn}$) are listed in italics.
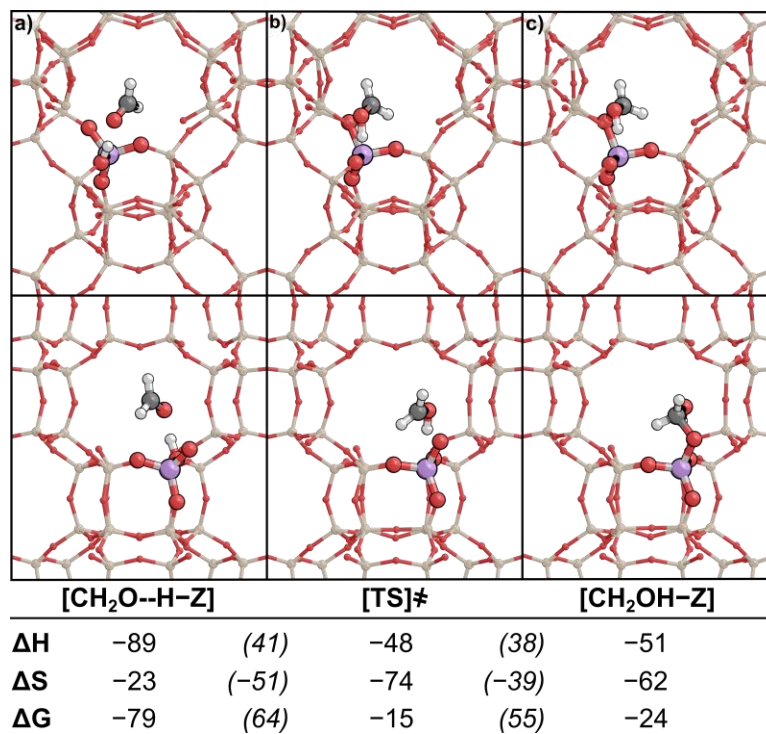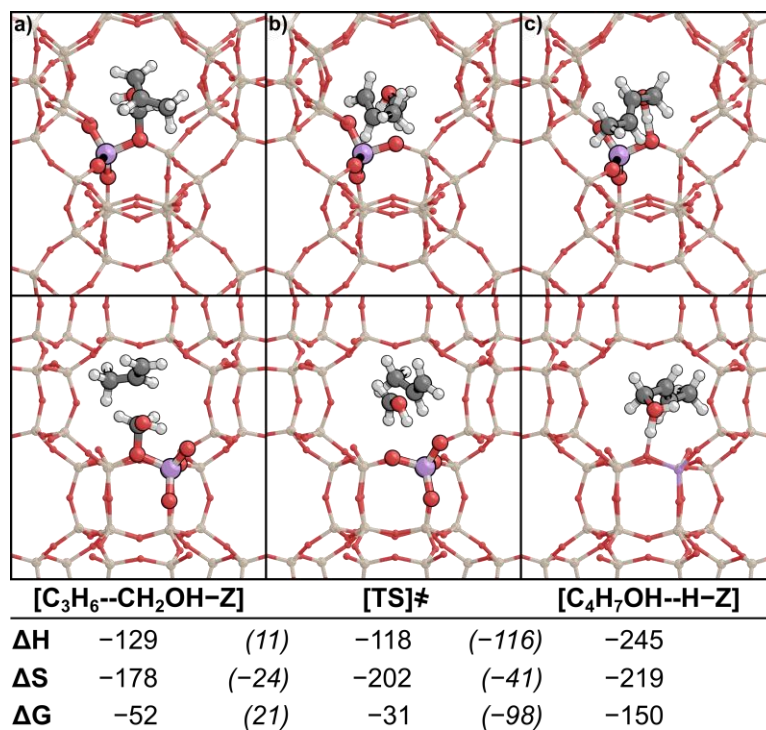
	[C$_4$H$_7$OH--H–Z]		[TS]‡		[H$_2$O--C$_4$H$_6$--H–Z]
ΔH	−245	*(130)*	−115	*(86)*	−159
ΔS	−219	*(18)*	−201	*(60)*	−159
ΔG	−150	*(122)*	−28	*(60)*	−90

	[H–Z]	[CH$_3$–Z]	[C4H6--H–Z]
ΔH	0	1	−117
ΔS	0	−5	−37
ΔG	0	3	−101

Figure S36. Additional states a) H–Z, b) CH$_3$–Z, and c) C$_4$H$_6$--H–Z in MFI. Enthalpy (ΔH), entropy (ΔS), and free energy (ΔG) values are reported at 433 K and relative to a protonated zeolite.

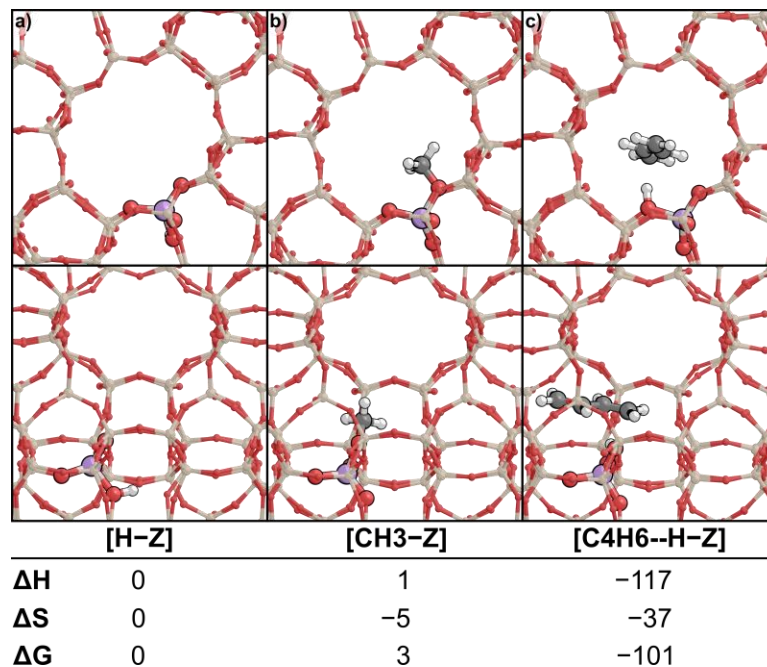|	[H−Z]	[CH3−Z]	[C4H6--H−Z]
ΔH	0	−16	−135
ΔS	0	−15	−41
ΔG	0	−10	−118

Figure S37. Additional states a) H–Z, b) CH$_3$–Z, and c) C$_4$H$_6$--H–Z in CHA. Enthalpy (ΔH), entropy (ΔS), and free energy (ΔG) values are reported at 433 K and relative to a protonated zeolite.
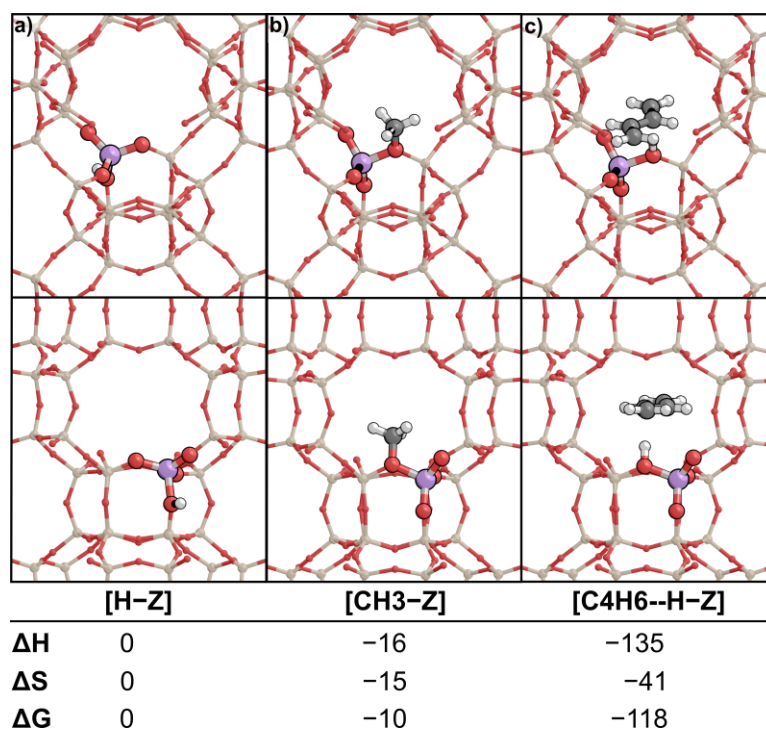
S11. Comparison of Alkene-mediated and CH₂O-mediated Pathway Barriers in CHA and MFI.

Table S3. Intrinsic (ΔG_{act}) and effective ($\Delta G^{\neq}$) free energy barriers for all reactions in the alkene-mediated and CH₂O-mediated pathways at 433 K. Effective barriers are relative to the protonated framework.

Reaction	ΔG_{act} $kJ\ mol^{-1}$		$\Delta G^{\neq}$ $kJ\ mol^{-1}$	
	MFI	*CHA*	*MFI*	*CHA*
C₂H₅–Z formation $C_2H_4^* \rightarrow C_2H_5-Z$	83	86	88	83
C₂H₅–Z formation with C₄H₈ $C_4H_8- C_2H_4^* \rightarrow C_4H_8- C_2H_5-Z$	83	84	125	97
C₂H₅–Z hydride transfer $C_4H_8- C_2H_5-Z \rightarrow C_2H_6- C_4H_6^*$	61	78	88	75
Concerted hydride transfer $C_4H_8- C_2H_4^* \rightarrow C_2H_6- C_4H_6^*$	55	74	98	87
CH₃–Z formation $CH_3OH^* \rightleftharpoons H_2O - CH_3-Z$	129	130	109	86
CH₂OH–Z formation $CH_3OH- CH_3-Z \rightarrow CH_4- CH_2OH-Z$	102	101	127	117
Concerted CH₂O formation $2CH_3OH^* \rightarrow CH_4- H_2O- CH_2O$	161	143	145	114
CH₂O protonation $CH_2O^* \rightarrow CH_2OH-Z$	69	64	−1	−15
Butenol formation $C_3H_6- CH_2OH-Z \rightarrow C_4H_8O^*$	32	21	−5	−31
Dehydration $C_4H_8O^* \rightarrow H_2O- C_4H_6^*$	79	122	−51	−28

S12. Discussion of Alkene-mediated Pathway Structures in CHA

The alkene-mediated pathway was investigated in the CHA framework via the same sequential (Eq. 2–3) and concerted mechanisms as in MFI (Eq. 1). The formation of C₂H₅–Z without co-adsorbed C₄H₈ occurs between O3 (protonation) and O1 (C–O bond formation) with a

ΔG_{act} of 86 kJ mol^{-1} and intrinsic barriers do not decrease with spectating C$_4$H$_8$ (Fig. 3b). The co-adsorption of C$_4$H$_8$ does not significantly alter the transition state structure or the intrinsic barrier (84 kJ mol^{-1}) for C$_2$H$_5$–Z formation, similar to the observations in MFI.

The transition state for hydride transfer between C$_4$H$_8$ and C$_2$H$_5$–Z, the second step in the sequential mechanism, occurs with a ΔG_{act} of 78 kJ mol^{-1} and the best structure is at O3 with C$_4$H$_8$ positioned directly above the carbocation (Fig. 3c). Similar to MFI, and as described in previous literature,(1–3) the transition state primarily involves cleavage of the C–O bond and formation of the hydride transfer complex. In CHA, the transition state forms at O3 in the large cage adjacent to the 8-MR. The transition state at O4, which has an energy 24 kJ mol^{-1} higher, also forms preferentially within an 8-MR, however C$_4$H$_8$ is rotated away from the C$_2$H$_5^+$ intermediate (Fig. S8). At O1, which is not located in an 8-MR, the transition state has an energy 60 kJ mol^{-1} higher (Fig. S8).

The concerted hydride transfer transition state is optimally protonated from O1 and located within the stabilizing 8-MR (Fig. 5d). Just as in MFI, where the C$_2$H$_5^+$ intermediate is stabilized by a second oxygen of the conjugate base, the transition state interacts with the negatively charged O3. The transition state at O1 is 7 kJ mol^{-1} higher in energy while the transition state at O3 has a ΔG_{act} 18 kJ mol^{-1} higher despite also being located in the 8-MR ring (Fig. S9)—demonstrating the necessity of testing multiple O-sites and configurations for each of these transition states.

S13. Discussion of CH$_2$O-mediated Structures in CHA

The formaldehyde mediated pathway was investigated in CHA, with the same sequential mechanism (Eqs. 5–6) and concerted mechanism (Eq. 7) as in MFI (Section 3.3). The dehydration of CH$_3$OH to form CH$_3$–Z, the first step of the sequential mechanism, has been computationally studied before using the PBE-D3 functional and found to occur with a ΔG_{act} of 171 kJ mol^{-1} at 673 K.(4) The most favorable transition state forms at O3 (Fig. 7a) with a ΔG_{act} of 130 kJ mol^{-1}, which is significantly lower than the previously reported value. The transition state is stabilized by dispersive interactions with the 8-MR and hydrogen bonding between H$_2$O and two framework oxygens (190 and 194 pm, Fig. 8a).

The formation of CH$_2$OH–Z from the reaction of CH$_3$OH with CH$_3$–Z preferentially forms at O4 (Fig. 8b) with a ΔG_{act} of 101 kJ mol^{-1} (nearly identical to that of MFI, ΔG_{act} 102 kJ mol^{-1}). The complex is also positioned adjacent to the 8-MR, to maximize dispersive forces, and hydrogen bonding between CH$_3$OH and a framework oxygen (185 pm, Fig. 8b) confers additional stability. The transition state at O1 experiences weaker framework interactions and has an energy 6 kJ mol^{-1} higher (Fig. S11), whereas the most favorable configuration at O2 has weaker hydrogen bonding (245 pm, Fig. S11) and an energy 7 kJ mol^{-1} higher.
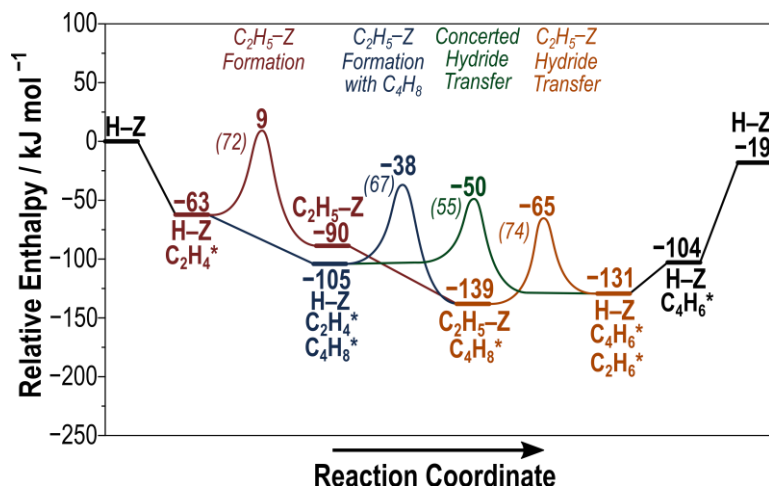
The concerted mechanism involves reacting two CH_3OH molecules simultaneously to form CH_2O. The transition state has a higher ΔG_{act} (143 kJ mol^{-1}) compared to the hydride transfer between CH_3OH with CH_3–Z (102 kJ mol^{-1}), despite the additional capacity for hydrogen bonding (184, 205, and 174 pm, Fig. 8c). The geometry of the concerted transition state is different than that of the sequential transition state and the CH_3^+ resides in the large cage of CHA where dispersive forces are weaker. As examined in MFI, the interconversion between CH_2OH–Z to form CH_2O+H–Z is relatively facile and occurs most favorably at O1 with a ΔG_{act} of 64 kJ mol^{-1} (Fig. 8d). Notably, CH_2O+H–Z has an energy 55 kJ mol^{-1} lower than CH_2OH–Z (Fig. 9), so formaldehyde most likely exists in the zeolite as CH_2O instead of a surface-bound species.

The reaction between CH_2OH–Z and propene to form butene-1-ol occurs with a ΔG_{act} of 21 kJ mol^{-1} at O3, where it experiences maximum stabilizing interactions within an 8-MR (Fig. 8e). The subsequent dehydration of butene-1-ol to form butadiene is most favorable at O3 and has a ΔG_{act} of 122 kJ mol^{-1} (Fig. 8f).

S14. Enthalpy Reaction Coordinate Diagrams

Figure S38. Reaction coordinate diagram of the sequential and concerted pathways for the alkene-mediated route in MFI. Enthalpies (kJ mol^{-1}, 433 K) relative to a bare acid site (proton) and stoichiometric amounts of gas-phase C_2H_4 and C_4H_8. Intrinsic free energy barriers are included in italics.
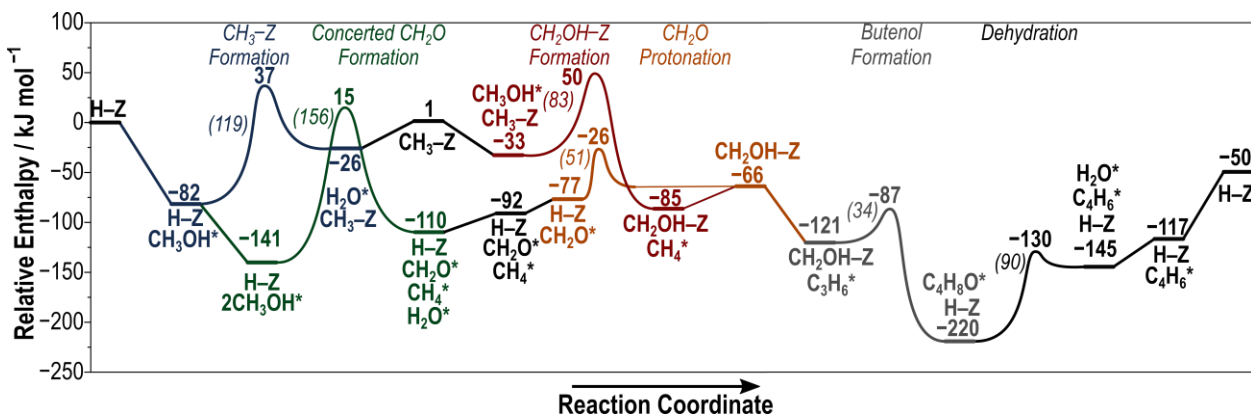
Figure S39. Reaction coordinate diagram of the sequential and concerted pathways for the alkene-mediated route in CHA. Enthalpies (kJ mol^{-1}, 433 K) relative to a bare acid site (proton) and stoichiometric amounts of gas-phase C_2H_4 and C_4H_8. Intrinsic free energy barriers are included in italics.
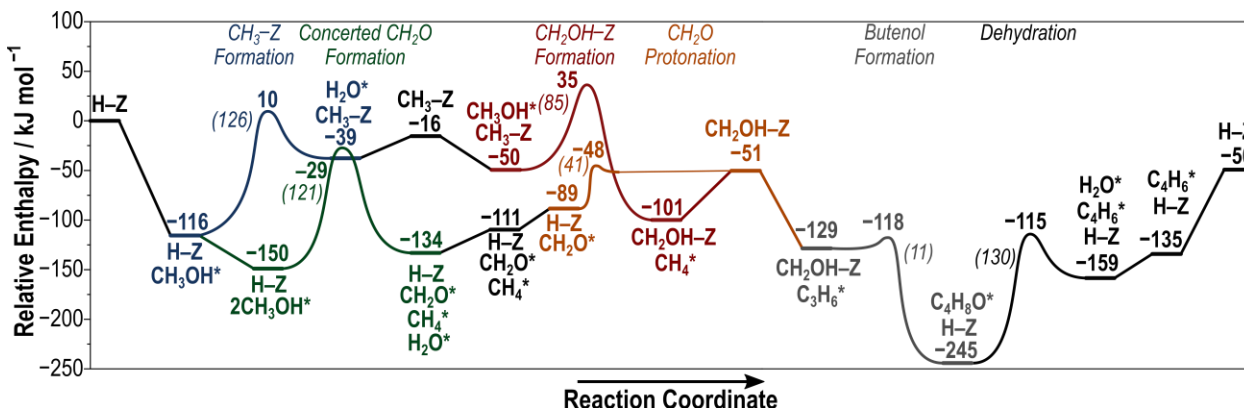

Figure S40. Reaction coordinate diagram of the sequential and concerted pathways for the CH_2O-mediated route in MFI. Enthalpies (kJ mol^{-1}, 433 K) relative to a bare acid site (proton) and stoichiometric amounts of gas-phase CH_3OH and C_3H_6. Intrinsic free energy barriers are included in italics.

Figure S41. Reaction coordinate diagram of the sequential and concerted pathways for the CH$_2$O-mediated route in CHA. Enthalpies (kJ mol^{-1}, 433 K) relative to a bare acid site (proton) and stoichiometric amounts of gas-phase CH$_3$OH and C$_3$H$_6$. Intrinsic free energy barriers are included in italics.

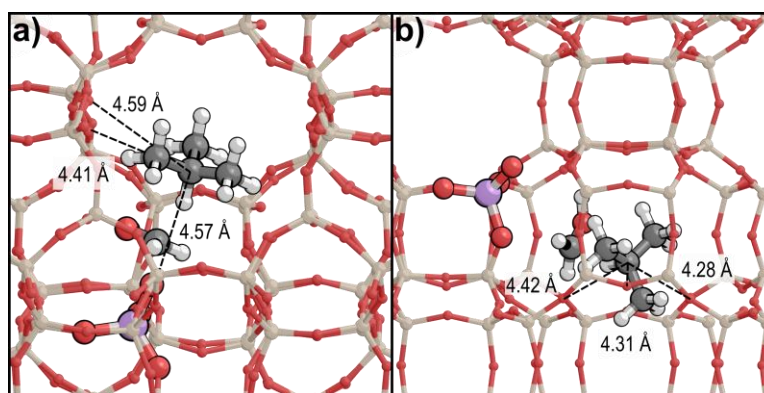*S15. Comparison of Hydride Transfer Between CH₃OH and Tert-butyl in MFI and CHA*

Figure S42. Transition state of the hydride transfer between tert-butyl–Z and CH$_3$OH in a) MFI and b) CHA. Distance (Å) between the tertiary tert-butyl carbon and the three closest framework atoms are labeled.
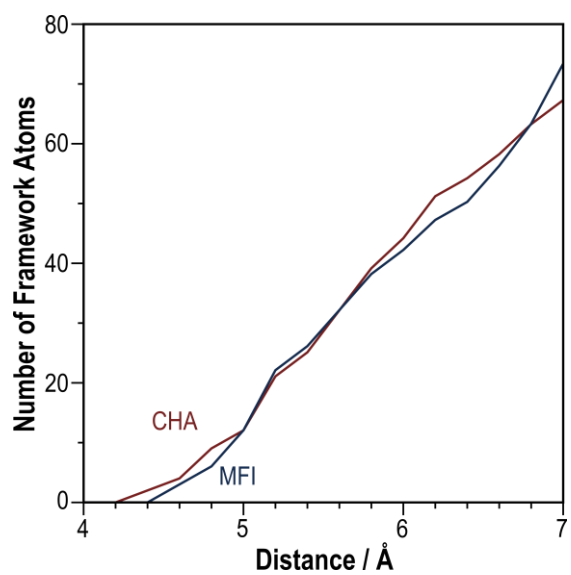
Figure S43. Number of framework atoms (Si, O, or Al) versus distance (Å) from the tertiary carbon atom of tert-butyl in the transition state of the hydride transfer with CH_3OH in MFI (blue) and CHA (red).

Table S4. The indices of O-atoms used in this work, and the corresponding index from the reference from which the MFI structure in this work was constructed, the T-sites bound to each O-atom, and the void environment to which each O-atom belongs.

O-atom		O-atom void environment[c]			T-atoms bound to O-atom	
This work[a]	van Koningsveld et. al.[b]	Int.	Str.	Sin.		
O1	O21	✓	✓		T1	T5
O2	O1	✓	✓	✓	T1	T2
O3	O15	✓		✓	T1	T10
O4	O16				T1	T4
O5	O2	✓	✓	✓	T2	T3
O6	O13		✓		T2	T8
O7	O6			✓	T2	T6
O8	O20	✓	✓	✓	T3	T12
O9	O3			✓	T3	T4
O10	O19		✓		T3	T6
O11	O17			✓	T4	T7
O12	O4			✓	T4	T5
O13	O5	✓	✓	✓	T5	T6
O14	O14		✓		T5	T11
O15	O18	✓	✓	✓	T6	T9
O16	O22	✓	✓		T7	T11
O17	O7	✓	✓		T7	T8
O18	O23	✓	✓	✓	T7	T7
O19	O8	✓	✓		T8	T9
O20	O12				T8	T12
O21	O25	✓		✓	T9	T9
O22	O9			✓	T9	T10
O23	O26	✓		✓	T10	T10
O24	O10				T10	T11
O25	O11	✓	✓		T11	T12
O26	O24	✓		✓	T12	T12

[a] From the numbering assigned by the International Zeolite Association (IZA).[74]

[b] From van Koningsveld, et. al.,[73] the source of the MFI structure used in this work.

[c] Intersection (int.), straight channel (str.), and sinusoidal channel (str.) void environments are denoted here for each O-atom based on the accessible locations around the atom and its ability to catalyze reactions in those environments.

S17. Maximum Rate Analysis and Relative Rates

Maximum rate analysis (MRA) examines each rate-determining step assuming every prior step is quasi-equilibrated, thus giving the highest possible rate of each step. The purpose of MRA is not to compare absolute rates of each reaction, nor is it to predict reaction rates comparable to measured data. Instead, our aim in this discussion is to compare relative rates of reactions and identify the rate-determining step of the reaction network. These rates are calculated with incomplete site balances (shown in Section S3 of the SI), and these site balances cancel out when comparing relative rates to identify the rate determining steps (Fig. 2b). We start by comparing the two C_2H_5–Z formation steps that occur in parallel, indicating that the step with the highest maximum rate is more likely to occur. C_2H_5–Z formation with spectating butene has a maximum rate are over 10^7-fold lower than rates without spectating butene (Fig. S44), indicating surface-bound ethyl formation occurs in the absence of co-adsorbed C_4H_8. Furthermore, the maximum rate of C_2H_5–Z formation with spectating C_4H_8 decreases with temperature (maximum rates are relative to a bare acid site, causing a negative enthalpy barrier) and this originates from an incomplete site balance—it is unlikely that these rates will decrease with temperature experimentally. Next, we compare the rate of C_2H_5–Z formation with the rate of hydride transfer, and, as these steps occur in series, the step with the lowest maximum rate will be rate determining. Because the sequential hydride transfer occurs with maximum rates over 10^2-times lower than C_2H_5–Z formation, the hydride transfer is the rate determining step of the sequential mechanism. Finally, we can compare the maximum rate of the sequential mechanism to the maximum rate of the concerted mechanism to determine the predominant hydride transfer route. For the same reasons discussed for C_2H_5–Z formation with spectating C_4H_8, both hydride transfer reaction rates have negative effective enthalpies and therefore decreasing rates with increasing temperature; however, it is unlikely this will occur experimentally. The rate of the sequential hydride transfer is 10-times faster than the rate of the concerted hydride transfer (Fig. S44), suggesting the sequential mechanism likely dominates with the hydride transfer as the rate determining step. However, because the transition states structures and maximum rates of the concerted and sequential hydride transfers are similar, these reaction mechanisms essentially indistinguishable.
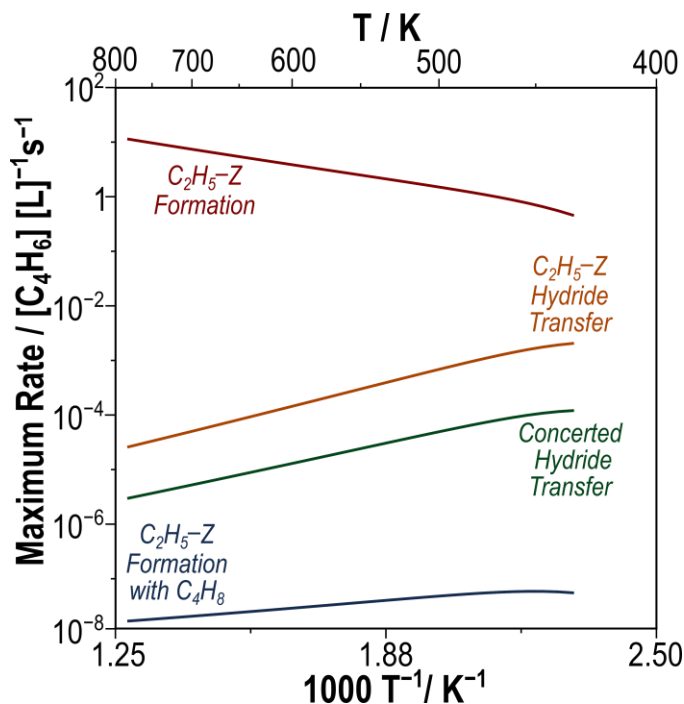
Figure S44. Maximum rate analysis of C_2H_5–Z formation (red), C_2H_5–Z formation with co-adsorbed C_4H_8 (blue), C_2H_5–Z hydride transfer (orange), and concerted hydride transfer (green) from 433–783 K at 0.004 bar C_2H_4 and 0.004 bar C_4H_8. Rates decreasing with temperature in this rate analysis stem from an incomplete site balance; however, this analysis is meant to compare relative rates not absolute rates.

Maximum rate analysis is again employed to find the rate determining step of the alkene-mediated pathway in CHA, using the same procedure as MFI. Comparing C_2H_5–Z formation with and without spectating C_4H_8, we find that co-adsorbed C_4H_8 lowers the rate by at least 10^4-fold (Fig. S45a). Just as in MFI, the effective enthalpy barrier for C_2H_5–Z formation with spectating C_4H_8 is negative relative to a bare acid site (-38 kJ mol^{-1}, Fig. 3b), therefore the maximum rate decreases as C_4H_8 adsorption becomes entropically limited at higher temperatures (Fig. S45a). Maximum rate analysis suggests the rate of hydride transfer is $>10^2$-fold slower than the rate of C_2H_5–Z formation all temperatures (Fig. S45a), indicating that the hydride transfer is the rate determining step of the sequential mechanism. Finally, we compare sequential and concerted hydride transfer routes and find that sequential hydride transfer occurs with a rate approximately 10 times faster than the concerted hydride transfer (Fig. S45a). We can repeat the same analysis with relative rates (Fig. S45b), which were calculated to remove the incomplete site balance present in maximum rates, to come to the same conclusions. All rates are relative to the slowest step according to maximum rate analysis, C_2H_5–Z formation with co-adsorbed C_4H_8. Following the same methodology, C_2H_5–Z hydride transfer governs the rate of the sequential mechanism because it has a relative rate $>10^2$-times slower than C_2H_5–Z formation (Fig. S45b). The rate determining step of the alkene-mediated pathway is C_2H_5–Z hydride transfer because it has a relative rate 10-times faster than the concerted hydride transfer (Fig. S45b).
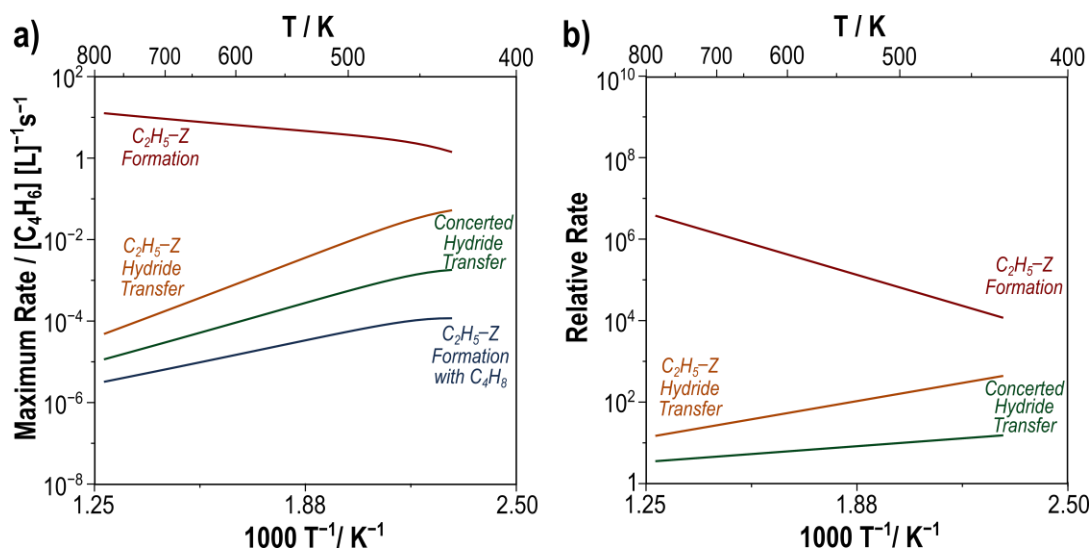
Figure S45. a) Maximum rate analysis of C_2H_5–Z formation (red), C_2H_5–Z formation with co-adsorbed C_4H_8 (blue), C_2H_5–Z hydride transfer (orange), and concerted hydride transfer (green) from 433–783 K at 0.004 bar C_2H_4 and 0.004 bar C_4H_8. Rates decreasing with temperature in this rate analysis stem from an incomplete site balance; however, this analysis is meant to compare relative rates not absolute rates. **b)** Rates of C_2H_5–Z formation (red), C_2H_5–Z hydride transfer (orange), and concerted hydride transfer (green) relative to the maximum rate of C_2H_5–Z formation with co-adsorbed C_4H from 433–783 K at 0.004 bar C_2H_4 and 0.004 bar C_4H_8.

For the CH_2O-mediated pathway, we start by comparing the maximum rates of CH_3–Z formation (Fig. S46, blue) and CH_2OH–Z formation (Fig. S46, red), as they occur in series in the sequential mechanism. CH_2OH–Z formation has a maximum rate 10-fold lower than CH_3–Z formation (Fig. S46) and is the rate determining step of the sequential mechanism. The maximum rate of CH_2OH–Z formation is subsequently compared to the maximum rate of concerted CH_2O formation (Fig. S46, green) to determine if the CH_2O-mediated pathway proceeds via the sequential or concerted mechanism. Because these steps occur in parallel, the one with the higher maximum rate indicates the prevailing mechanism; CH_2OH–Z formation has a maximum rate $>10^4$-fold faster than concerted CH_2O formation (Fig. S46), therefore formaldehyde is formed by the sequential mechanism. The maximum rate of CH_2OH–Z formation is compared to the maximum rate of the remaining steps: CH_2O protonation, butenol formation, and dehydration. All of these steps occur in series and have maximum rates $>10^{10}$-fold faster than CH_2OH–Z formation (Fig. S46), therefore CH_2OH–Z formation is the rate determining step of the CH_2O-mediated pathway.
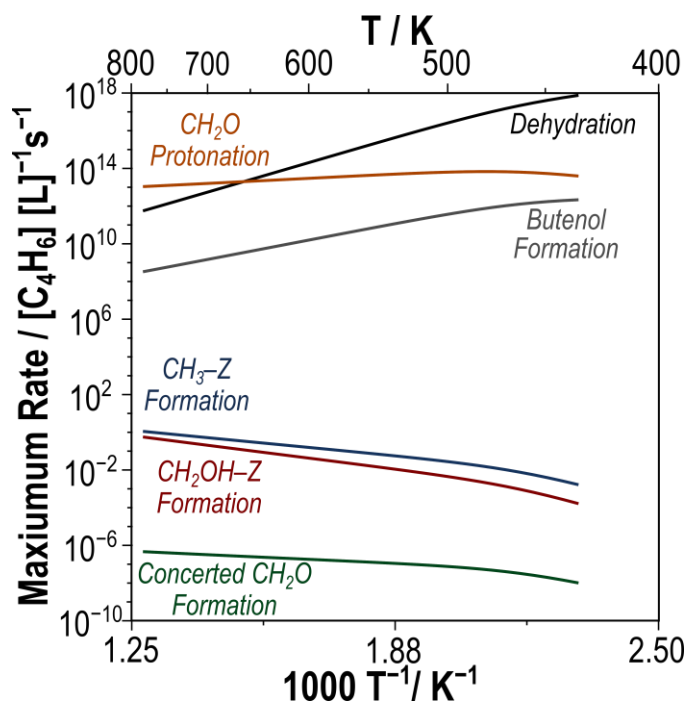
Figure S46. Maximum rates of the CH_2O-mediated route in MFI from 433–783 K at 0.1 bar CH_3OH, 0.01 bar H_2O, 0.01 bar CH_4, and 0.1 bar C_3H_6 with CH_3–Z formation (blue), CH_2OH–Z formation (red), concerted CH_2O formation (green), CH_2O protonation (orange), butenol formation (gray), and butenol dehydration (black) as the rate determining step. Rates decreasing with temperature in this rate analysis stem from an incomplete site balance; however, this analysis is meant to compare relative rates not absolute rates. Rate equations are defined in Section S3.

In CHA, we again conclude that CH_2O is formed via the sequential mechanism and that the hydride transfer is the rate determining step, as it occurs with a maximum rate >10-fold lower than CH_3–Z formation (Fig. S47a, blue) but >10^2-fold higher than CH_2O formation (Fig. S47a, red). Compared to the maximum rate of CH_2OH–Z formation, the maximum rates of the remaining steps (CH_2O protonation, butenol formation, and dehydration) are >10^8-fold higher (Fig. S47a). Consistent with what is observed in MFI, the rate determining step of the CH_2O-mediated pathway in CHA is the hydride transfer of CH_2OH–Z formation. Relative rates were also calculated relative to the step with the slowest maximum rate (concerted CH_2O formation) to remove the incomplete site balance in the maximum rates. Relative rates can be analyzed the same way as maximum rates to come to the same conclusion regarding the mechanism by which the CH_2O-mediated route proceeds. Formaldehyde is formed via the sequential mechanism, and the rate of formaldehyde formation is controlled by CH_2OH–Z formation because it has a relative rate >10-times slower than CH_3–Z formation (Fig. 47b). CH_2O protonation, butenol formation, and dehydration have relative rates >10^8-times faster (Fig. S47b) than CH_2OH–Z formation, therefore the rate of the CH_2O-mediated pathway in CHA is governed by the rate of CH_2OH–Z formation.
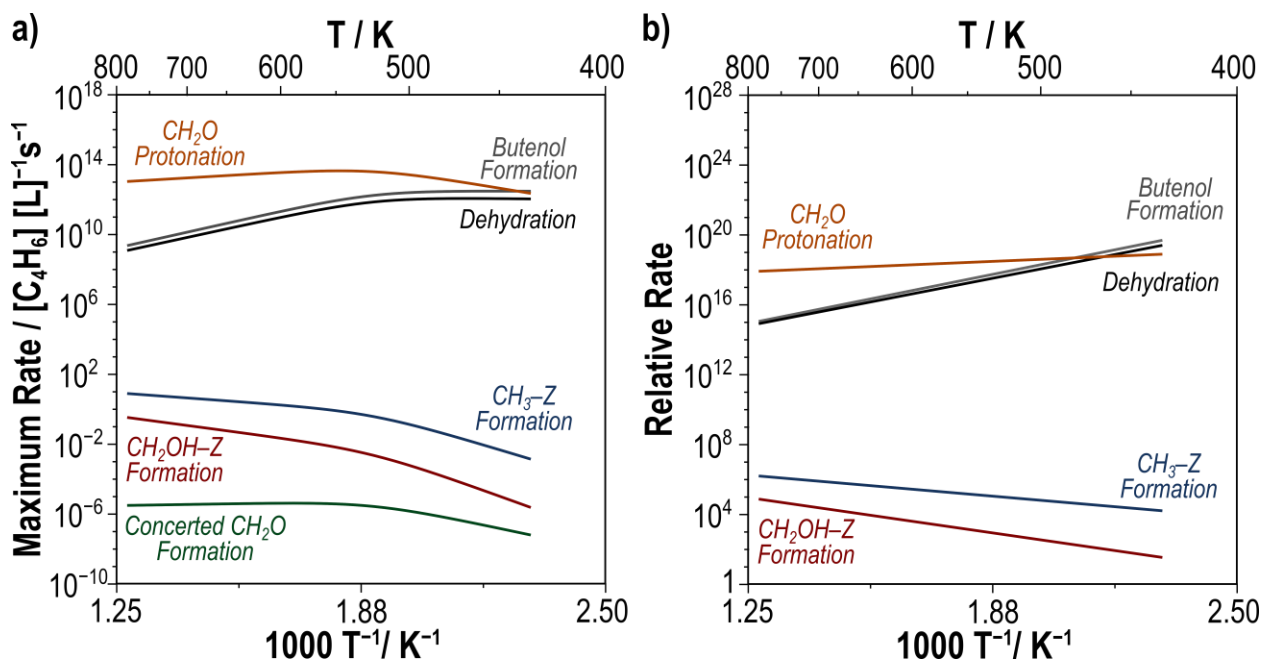
Figure S47. a) Maximum rates of the CH_2O-mediated route in CHA from 433–783 K at 0.1 bar CH_3OH, 0.01 bar H_2O, 0.01 bar CH_4, and 0.1 bar C_3H_6 with CH_3–Z formation (blue), CH_2OH–Z formation (red), concerted CH_2O formation (green), CH_2O protonation (orange), butenol formation (gray), and butenol dehydration (black) as the rate determining step. b) Rates of CH_3–Z formation (blue), CH_2OH–Z formation (blue), CH_2O protonation (orange), butenol formation (gray), and dehydration (black) relative to the rate of concerted CH_2O formation, the lowest rate according to maximum rate analysis, from 433–783 K at 0.1 bar CH_3OH, 0.01 bar H_2O, 0.01 bar CH_4, and 0.1 bar C_3H_6. Rates decreasing with temperature in this rate analysis stem from an incomplete site balance; however, this analysis is meant to compare relative rates not absolute rates. Rate equations are defined in Section S3.